Unconventional Superconducting Pairing Symmetries in $La_3Ni_2O_7$: from the Perspective of Topology

Guan-Hao Feng,[1,*] Jun Quan,[2,1,†] and Yusheng Hou[3]

[1] *School of Physical Science and Technology, Lingnan Normal University, Zhanjiang, 524048, China*
[2] *School of Physics, Changchun Normal University, Changchun, 130032, China*
[3] *Guangdong Provincial Key Laboratory of Magnetoelectric Physics and Devices, Center for Neutron Science and Technology, School of Physics, Sun Yat-Sen University, Guangzhou, 510275, China*

(Dated: June 3, 2025)

The recently discovered superconductor $La_3Ni_2O_7$ has attracted significant attention due to its remarkably high T_c and unconventional pairing mechanism. High-pressure experiments have demonstrated that the emergence of the superconducting phase is associated with a transition to a higher-symmetry structure. Motivated by this observation, we investigate superconductivity in $La_3Ni_2O_7$ under high pressure from the perspectives of symmetry and topology. Based on a bilayer two-orbital model with Ni-$d_{3z^2-r^2}$ and $d_{x^2-y^2}$ orbitals, we systematically examine all symmetry-allowed multi-orbital superconducting pairings at the Bogoliubov-de Gennes (BdG) mean-field level, including terms up to next-nearest neighbors. By solving the self-consistent gap equations and analyzing the BdG condensation energies, we find that the A_{1g} pairing channel is the most probable one. The dominant pairing is $s_{\pm}$-wave, originating from the intra-orbital interaction of the bilayer Ni-$d_{3z^2-r^2}$ orbital, while the subdominant pairing is $d_{x^2-y^2}$-wave, arising from the inter-orbital interactions between the $d_{3z^2-r^2}$ and $d_{x^2-y^2}$ orbitals. Furthermore, we implement the theory of symmetry indicator to reveal the topological characteristics of each pairing channel, demonstrating that the pairing symmetries can be identified by their distinct topological features.

Introduction.- The bilayer Ruddlesden-Popper compound $La_3Ni_2O_7$ exhibits a high onset superconducting transition temperature ($T_c \approx 80\ K$) under moderate pressures, which has recently attracted significant attention [1–21]. Comprehensive high-pressure experiments up to 104 GPa have revealed that the superconducting phase transition is accompanied by a structural phase transition from $Amam$ to $I4/mmm$ above 10 GPa [16, 17, 22]. The superconducting pairing symmetry and mechanism related to this structural transition remain a major challenge in uncovering the origin of the remarkably high T_c. Nevertheless, experimental investigations into the properties of the superconductivity have provided some clues to this problem. First, the high T_c exhibits remarkable robustness under applied magnetic fields and remains unaffected by the low superconducting volume fraction [12–20]. This implies a short superconducting coherence length. Second, no evidence of long-range magnetic order was observed in powder neutron diffraction measurements [4, 23]. This suggests that time-reversal symmetry is likely preserved, or that only minor magnetic moments may exist. Third, the maximum superconducting volume fraction reported is approximately 48%, indicating that superconductivity originates from the bilayer $La_3Ni_2O_7$ phase [17]. Fourth, samples of varying quality exhibit a linear-T dependence of resistivity, which is typically regarded as a signature of strong electronic correlations and suggests an unconventional nature of superconductivity [12, 20, 24].

Based on the experimental findings described above, various theories have been proposed to elucidate the underlying pairing mechanism. Numerous theories suggest that strong vertical inter-layer antiferromagnetic interactions between the bilayer Ni-$d_{3z^2-r^2}$ orbitals drive the superconductivity [25–30]. In these scenarios, Cooper pairs predominantly form on the Ni-$d_{3z^2-r^2}$ orbitals, which are associated with the γ-sheet of the Fermi surface, while other models attribute the pairing to the α and β bands [29, 31–33]. A variety of theoretical approaches, such as functional renormalization group calculations, random phase approximation, and mean-field theory, have been employed. The resulting possible pairing symmetries are believed to be $s_{\pm}$ [25, 28, 30, 34–42] and d-wave [29, 31–33, 43–47]. However, at the BdG mean-field level, a specific self-consistent solution converging to a symmetry-allowed form is still lacking. It is therefore important to ask whether this multi-orbital unconventional superconductor can be understood within the BdG mean-field theory as the anisotropic pairings in cuprate and iron-based superconductors.

In this Letter, we systematically investigate the possible superconducting pairing symmetries at the BdG mean-field level. Given that experiments indicate a short superconducting coherence length, we consider candidate superconducting pairings up to next-nearest-neighbor terms. The bilayer $La_3Ni_2O_7$ under high pressure is expected to respect the symmetries of the non-magnetic Type-II LG $p4/mmm1'$, which can be subduced from $I4/mmm1'$. Thus, all symmetry-allowed pairings can be identified by the numerical methods with the Qsymm software package [48]. By solving the self-consistent BCS gap equation and analyzing the BdG condensation energy, we demonstrate that the most probable pairing channel is A_{1g}, with a dominant $s_{\pm}$-wave character and a

competing subdominant $d_{x^2-y^2}$-wave component. Moreover, we employ theory of symmetry indicator (SI) [49–55] to investigate the topological features induced by the possible unconventional pairing symmetries. Our results support the BdG mean-field theory for bilayer $La_3Ni_2O_7$ under high pressure.

Model.- To illustrate the idea, we begin with the crystal structure of $La_3Ni_2O_7$ under high pressure from the recent experiments. We construct a two-orbital (Ni-$d_{3z^2-r^2}$ and $d_{x^2-y^2}$) convention-II tight-binding model on a bilayer square lattice, respecting the symmetries of Type-II LG ($p4/mmm1'$). This model is derived via Wannier downfolding of the DFT+U band structure and is given by

$$\begin{aligned}
&\mathcal{H}_{\boldsymbol{k}} - \mu \\
&= (\epsilon^z + 2t_1^z(\cos k_x + \cos k_y) \\
&+ 4t_2^z \cos k_x \cos k_y)\,\rho_0 \frac{\sigma_0+\sigma_z}{2} s_0 \\
&+ (\epsilon^x + 2t_1^x(\cos k_x + \cos k_y) \\
&+ 4t_2^x \cos k_x \cos k_y)\,\rho_0 \frac{\sigma_0-\sigma_z}{2} s_0 \\
&+ 2t_3^{xz}(-\cos k_x + \cos k_y)\rho_0\sigma_x s_0 \\
&+ (2t_\perp^x(\cos k_x + \cos k_y) + \epsilon_\perp^x)\,\rho_x \frac{\sigma_0+\sigma_z}{2} s_0 \\
&+ 2t_4^{xz}(-\cos k_x + \cos k_y)\,\rho_x\sigma_x s_0 \\
&+ \epsilon_\perp^z \rho_x \frac{\sigma_0-\sigma_z}{2} s_0, \qquad (1)
\end{aligned}$$

where ρ_i, σ_i, and s_i $(i = 0, x, y, z)$ are the Pauli matrices for the layer, orbital, and spin degrees of freedom, respectively. The basis operator used here is $\psi^\dagger_{k\sigma} = \left[c^\dagger_{Az\uparrow}, c^\dagger_{Az\downarrow}, c^\dagger_{Ax\uparrow}, c^\dagger_{Ax\downarrow}, c^\dagger_{Bz\uparrow}, c^\dagger_{Bz\downarrow}, c^\dagger_{Bx\uparrow}, c^\dagger_{Bx\downarrow}\right]$, where A and B label the bilayer, and x and z denote $d_{x^2-y^2}$ and $d_{3z^2-r^2}$ orbital, respectively. We have adopted the conventional lattice basis here and considered up to the next-nearest-neighbor hoppings, since the resulting Fermi surface is sufficient to capture the topological properties of the superconducting system, as shown in Fig. 1(a). The parameter values of this normal-state Hamiltonian are provided in Supplementary Note 17 [56]. This minimal two-orbital model closely follows that of Luo et al. [57], and we adopt the same parameter notation here. However, we consider an effective Hubbard $U = 3.5$ eV to account for the correlation effects of the $3d$ electrons in the Ni atoms.

In multi-orbital superconducting systems, strong inter-orbital electron correlations must be taken into account when determining the symmetries of the superconducting pairings. In the absence of long-range magnetic order, as evidenced by neutron diffraction and inelastic neutron scattering experiments down to a temperature of 10 K [4, 23], the superconducting pairing is believed to arise from spin fluctuations [29, 40, 42]. These strong interactions should be effectively attractive and preserve the symmetries of non-magnetic LG $p4/mmm1'$. Thus, we introduce the extended multi-orbital attractive Hubbard interactions, which take a factorizable form,

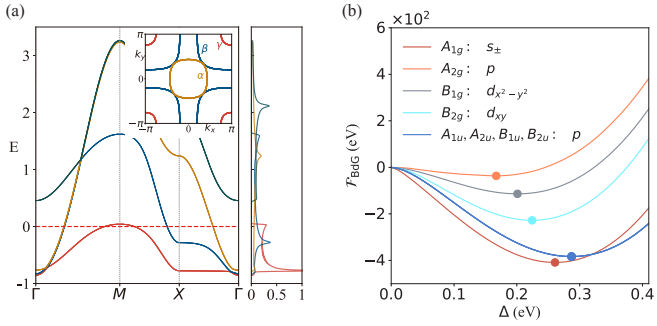

Figure 1. (a) Band structure of the bilayer tight-binding model in Eq. 1. The subfigures show the Fermi surface and the normalized DOS of each band. (b) Comparison of BdG condensation energies of the dominant pairings across the eight real one-dimensional representation pairing channels. The point inside each curve is the saddle-point solution of the corresponding BCS gap equation.

$$H_{\mathrm{attr}} = \sum_{\boldsymbol{k}\boldsymbol{k}'\alpha\beta ss'} V_{\mathrm{eff}} c^\dagger_{\boldsymbol{k}\alpha s} c^\dagger_{-\boldsymbol{k}\beta s'} c_{-\boldsymbol{k}'\beta s'} c_{\boldsymbol{k}'\alpha s}, \qquad (2)$$

where $V_{\mathrm{eff}} = \frac{-V_{\alpha\beta ss'}}{N} e^{-i(\boldsymbol{k}-\boldsymbol{k}')\cdot \boldsymbol{r}_{\alpha\beta ss'}}$, with s and s' representing the spin degrees of freedom, while α and β denoting the degrees of freedom other than spin. Here, N is the number of discrete momentum points $\boldsymbol{k}$ (or $\boldsymbol{k}'$); $V_{\alpha\beta ss'}$ is the strength of the attractive potential; and the phase factor $e^{-i(\boldsymbol{k}-\boldsymbol{k}')\cdot \boldsymbol{r}_{\alpha\beta ss'}}$ arises from the Fourier transform of the Cooper pair creation operator $c^\dagger_{\boldsymbol{k}\alpha s} c^\dagger_{-\boldsymbol{k}\beta s'}$ and annihilation operator $c_{-\boldsymbol{k}'\beta s'} c_{\boldsymbol{k}'\alpha s}$. We then carry out the Hubbard–Stratonovich decoupling [56] and obtain the mean-field pairing potential

$$H^{\mathrm{MF}}_{\mathrm{attr}} = H_\Delta + \sum_{\alpha\beta ss'} \frac{N}{V_{\alpha\beta ss'}} \Delta^*_{\alpha\beta ss'} \Delta_{\alpha\beta ss'} \qquad (3)$$

$$\begin{aligned}
H_\Delta = \sum_{\boldsymbol{k}\alpha\beta ss'} \big(&\Delta^*_{\alpha\beta ss'} e^{i\boldsymbol{k}\cdot\boldsymbol{r}_{\alpha\beta}} c_{-\boldsymbol{k}\beta s'} c_{\boldsymbol{k}\alpha s} \\
&+ \Delta_{\alpha\beta ss'} e^{-i\boldsymbol{k}\cdot\boldsymbol{r}_{\alpha\beta}} c^\dagger_{\boldsymbol{k}\alpha s} c^\dagger_{-\boldsymbol{k}\beta s'}\big). \qquad (4)
\end{aligned}$$

The combination of the terms $\Delta^*_{\alpha\beta ss'} e^{i\boldsymbol{k}\cdot\boldsymbol{r}_{\alpha\beta ss'}}$ in H_Δ can result in various pairing symmetries, including $s_\pm$, $p_x \pm ip_y$, $d_{x^2-y^2}$, and d_{xy}. The favored pairing symmetry is then determined by the free energy using the standard expression [56, 58, 59]

$$\mathcal{F}_{\mathrm{S}} = \frac{Nn}{V} |\Delta|^2 - 2k_B T \sum_{k\alpha} \ln\left[2\cosh(\beta E^{\mathrm{BdG}}_{\boldsymbol{k}\alpha}/2)\right], \qquad (5)$$

where the energy eigenvalues of the BdG Hamiltonian are denoted as $\pm E^{\mathrm{BdG}}_{\boldsymbol{k}\alpha}$, and $\beta = 1/k_B T$ is the inverse

temperature. The elements $\Delta_{\alpha\beta ss'}$ with the same value Δ together form the pairing gap matrix $\tilde{\Delta}$ in the Nambu basis. Here, n is the number of elements in $\tilde{\Delta}$. When $\Delta = 0$, Eq. 5 reduces to the free energy $\mathcal{F}_{\rm N}$ of the normal state. The equilibrium gap value $\Delta = \Delta_{\alpha\beta ss'}$ can be identified by minimizing $\mathcal{F}_{\rm S}$ with respect to Δ^*, which leads to the self-consistent BCS gap equation

$$\Delta = -\frac{V}{Nn}\sum_{\boldsymbol{k}} \mathrm{Tr}\left[\frac{\partial \mathcal{H}^{\rm BdG}_{\boldsymbol{k}}}{\partial \Delta} U_{\boldsymbol{k}} n_F(E^{\rm BdG}_{\boldsymbol{k}}) U^{\dagger}_{\boldsymbol{k}}\right], \quad (6)$$

where n_F is a diagonal matrix whose entries are the Fermi distribution functions for the eigenvalues $E^{\rm BdG}_{\boldsymbol{k}}$. Here $U_{\boldsymbol{k}}$ is the unitary matrix that diagonalizes the BdG Hamiltonian. Once the strength of the potential V is specified, the mean-field saddle-point solution for Δ can be obtained. The favored pairing symmetry can then be determined by comparing the BCS condensation energies, $\mathcal{F}_{\rm BdG} = \mathcal{F}_{\rm S} - \mathcal{F}_{\rm N}$.

When considering pairings up to the next-nearest neighbors, the number of the symmetry-allowed pairings H_Δ is limited, which can be systematically identified using the numerical methods with the generators of BdG Hamiltonian in different pairing channels [56] and Qsymm software package [48]. The favored pairing states can subsequently be determined by solving the self-consistent gap equations in Eq. 6 and performing a BdG condensation energy analysis with Eq. 5, as summarized in Tab. I.

Topological Classification.- Following the Altland-Zirnbauer (AZ) ten-fold way classification, the superconducting states of spinful ($\mathcal{T}^2 = -1$) electronic systems can be categorized as either class DIII ($\mathcal{P}^2 = +1$) or CII ($\mathcal{P}^2 = -1$). In light of the difficulties in experimentally realizing class CII superconductors in electronic systems [60], we restrict our analysis to class DIII. Under high pressure, the crystal structure of bilayer $La_3Ni_2O_7$ exhibits the symmetries of Type-II LG $p4/mmm1'$. The corresponding point group is $4/mmm$ (D_{4h}), which possesses eight real $1D$ representations: A_{1g}, A_{2g}, B_{1g}, B_{2g}, A_{1u}, A_{2u}, B_{1u}, B_{2u}, and two $2D$ representations: E_g, E_u. Since time-reversal symmetry is preserved in the superconducting phase, the pairings must belong to one of the $1D$ pairing channels [61–63].

The anisotropic pairing potential may not open gaps to all three Fermi surfaces, leading to the emergence of topological nodal phases. In the presence of inversion symmetry, the band nodes can be classified according to the combined symmetries $\mathfrak{T} = \mathcal{T}\mathcal{I}$, $\mathfrak{P} = \mathcal{P}\mathcal{I}$, and the chiral symmetry $\mathcal{C}$. This is known as the centrosymmetric extension of AZ classification (AZ+I classification) [64]. Note that the pairing channels with $\chi_{\{-1|0\}} = +1$ satisfy the commutation relation $[\mathcal{P}, \mathcal{I}] = 0$, which leads to $\mathfrak{P}^2 = +1$. These systems fall into class DIII, supporting topologically protected $2\mathbb{Z}$ nodal points [64]. In contrast, the pairing channel with $\chi_{\{-1|0\}} = -1$ satisfies the anti-commutation relation $\{\mathcal{P}, \mathcal{I}\} = 0$, resulting in $\mathfrak{P}^2 = -1$, and such systems fall into class CII without topological nodes.

For the bands satisfying the insulating compatibility relations of Type-II LG $p4/mmm1'$, the original SI group is $X_{\rm BS} = \mathbb{Z}_4$ (see Supplementary Note 4 for details [56]). When the bands are fully gapped throughout the first Brillouin zone, the z_4 invariant corresponds to the mirror Chern number. When the system is gapless, the nontrivial z_4 indicates the existence of topologically protected nodes. The original SIs can also be used to indicate topological superconducting states by neglecting particle-hole symmetry (PHS). However, the presence of PHS implies that the topological properties of superconducting states should be determined by both positive and negative-energy quasiparticles. Since the symmetry indicators are linear functions of the symmetry data vectors of the bands, the overall band topology can be regarded as a stacking of the topological properties of individual bands that satisfy the insulating compatibility relations. In this way, the two bands closest to $E = 0$ determine whether the quasiparticle spectrum is gapped or gapless, while the other bands determine the edge states. Thus we can obtain the following equations:

$$z_4^{\rm nodal} = z_4^{(1)} + \bar{z}_4^{(1)} \mod 4, \quad (7)$$

$$z_4^{\rm edge} = z_4 - z_4^{\rm nodal} \mod 4, \quad (8)$$

where $z_4^{(1)} = z_4(B^{(1)})$ is the original SI for the first band below $E = 0$ and $\bar{z}_4^{(1)}$ is the original SI for the first band above $E = 0$. When $z_4^{\rm nodal}$ takes a nontrivial value, the system is necessarily gapless, featuring topologically charged nodes in the bulk spectrum.

The theory of original SI may have difficulty in identifying higher-order TSC phases. Alternatively, the refined SI provides a reliable approach to address this limitation [60, 65]. Therefore, for completeness, we also calculate the refined SIs. For the A_{1g}/A_{2g} pairing channels, the refined SI group is trivial; For the B_{1g}/B_{2g} pairing channels, the refined SI group is $X^{\rm BdG}_{\rm BS} = \mathbb{Z}_2 \times \mathbb{Z}_2$, while for the A_{1u}/A_{2u} and B_{1u}/B_{2u} pairing channels, the refined SI groups are both $X^{\rm BdG}_{\rm BS} = \mathbb{Z}_2 \times \mathbb{Z}_8$. This is because the refined elementary band representation matrices in these pairing channels differ only by a permutation transformation, which preserves the Smith normal forms. The results of topological classification are summarized in Supplementary Note 3 [56].

Nodal superconducting phases.- According to the AZ+I classification, the pairing channels with $\chi_{\{-1|0\}} = +1$ belong to class DIII and support topological nodal points, which are characterized by a $2\mathbb{Z}$-valued π_1-charge corresponding to the usual winding number. The non-

Table I. The dominant and subdominant pairings in different channels.

$4/mmm(D_{4h})$	Dominant	Subdominant
A_{1g}	$\Delta_8\left[(\cos k_x+\cos k_y)\,\tau_y\rho_0(\sigma_0+\sigma_z)s_y\right]$ $\Delta_{10}\left[(\cos k_x+\cos k_y)\,\tau_y\rho_x(\sigma_0+\sigma_z)s_y\right]$	$2\Delta_9\left[(\cos k_x-\cos k_y)\,\tau_y\rho_0\sigma_x s_y\right]$ $2\Delta_{11}\left[(\cos k_x-\cos k_y)\,\tau_y\rho_0\sigma_x s_y\right]$
A_{2g}	$\Delta_3\left[\sin k_x\tau_x\rho_z(\sigma_0-\sigma_z)s_z+\sin k_y\tau_y\rho_z(\sigma_0-\sigma_z)s_0\right]$	$4\Delta_6\sin k_x\sin k_y\tau_y\rho_0\sigma_x s_y$ $4\Delta_7\sin k_x\sin k_y\tau_y\rho_x\sigma_x s_y$
B_{1g}	$\Delta_6\left[(\cos k_x-\cos k_y)\,\tau_y\rho_0(\sigma_0+\sigma_z)s_y\right]$ $\Delta_8\left[(\cos k_x-\cos k_y)\,\tau_y\rho_x(\sigma_0+\sigma_z)s_y\right]$	$\Delta_{10}\left[(\cos k_x-\cos k_y)\,\tau_y\rho_0(\sigma_0-\sigma_z)s_y\right]$ $\Delta_{11}\left[(\cos k_x+\cos k_y)\,\tau_x\rho_y(\sigma_0+\sigma_z)s_x\right]$
B_{2g}	$2\Delta_8\sin k_x\sin k_y\tau_y\rho_0(\sigma_0+\sigma_z)s_y$ $2\Delta_9\sin k_x\sin k_y\tau_y\rho_x(\sigma_0+\sigma_z)s_y$	$2\Delta_{10}\sin k_x\sin k_y\tau_y\rho_0(\sigma_0-\sigma_z)s_y$ $2\Delta_{11}\sin k_x\sin k_y\tau_y\rho_x(\sigma_0-\sigma_z)s_y$
A_{1u}	$\Delta_2\left[\sin k_x\tau_x\rho_0(\sigma_0+\sigma_z)s_z+\sin k_y\tau_y\rho_0(\sigma_0+\sigma_z)s_0\right]$ $\Delta_4\left[\sin k_x\tau_x\rho_x(\sigma_0+\sigma_z)s_z+\sin k_y\tau_y\rho_x(\sigma_0+\sigma_z)s_0\right]$	$\Delta_6\left[\sin k_x\tau_x\rho_0(\sigma_0-\sigma_z)s_z+\sin k_y\tau_y\rho_0(\sigma_0-\sigma_z)s_0\right]$ $\Delta_7\left[\sin k_x\tau_x\rho_x(\sigma_0-\sigma_z)s_z+\sin k_y\tau_y\rho_x(\sigma_0-\sigma_z)s_0\right]$
A_{2u}	$\Delta_2\left[\sin k_x\tau_y\rho_0(\sigma_0+\sigma_z)s_0-\sin k_y\tau_x\rho_0(\sigma_0+\sigma_z)s_z\right]$ $\Delta_4\left[\sin k_x\tau_y\rho_x(\sigma_0+\sigma_z)s_0-\sin k_y\tau_x\rho_x(\sigma_0+\sigma_z)s_z\right]$	$\Delta_6\left[\sin k_x\tau_y\rho_0(\sigma_0-\sigma_z)s_0-\sin k_y\tau_x\rho_0(\sigma_0-\sigma_z)s_z\right]$ $\Delta_7\left[\sin k_x\tau_y\rho_x(\sigma_0-\sigma_z)s_0-\sin k_y\tau_x\rho_x(\sigma_0-\sigma_z)s_z\right]$
B_{1u}	$\Delta_2\left[\sin k_x\tau_x\rho_0(\sigma_0+\sigma_z)s_z-\sin k_y\tau_y\rho_0(\sigma_0+\sigma_z)s_0\right]$ $\Delta_4\left[\sin k_x\tau_x\rho_x(\sigma_0+\sigma_z)s_z-\sin k_y\tau_y\rho_x(\sigma_0+\sigma_z)s_0\right]$	$\Delta_6\left[\sin k_x\tau_x\rho_0(\sigma_0-\sigma_z)s_z-\sin k_y\tau_y\rho_0(\sigma_0-\sigma_z)s_0\right]$ $\Delta_7\left[\sin k_x\tau_x\rho_x(\sigma_0-\sigma_z)s_z-\sin k_y\tau_y\rho_x(\sigma_0-\sigma_z)s_0\right]$
B_{2u}	$\Delta_2\left[\sin k_x\tau_y\rho_0(\sigma_0+\sigma_z)s_0+\sin k_y\tau_x\rho_0(\sigma_0+\sigma_z)s_z\right]$ $\Delta_4\left[\sin k_x\tau_y\rho_x(\sigma_0+\sigma_z)s_0+\sin k_y\tau_x\rho_x(\sigma_0+\sigma_z)s_z\right]$	$\Delta_6\left[\sin k_x\tau_y\rho_0(\sigma_0-\sigma_z)s_0+\sin k_y\tau_x\rho_0(\sigma_0-\sigma_z)s_z\right]$ $\Delta_7\left[\sin k_x\tau_y\rho_x(\sigma_0-\sigma_z)s_0+\sin k_y\tau_x\rho_x(\sigma_0-\sigma_z)s_z\right]$

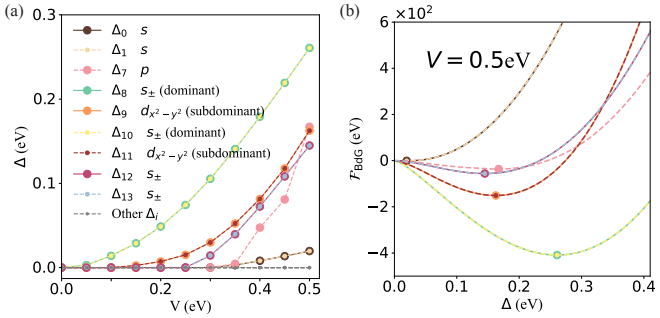

Figure 2. (a) Pairing strength Δ_i vs V_i obtained by solving the self-consistent BCS gap equations Eq. 6 in the A_{1g} pairing channel. (b) BdG condensation energy $\mathcal{F}_{\rm BdG}$ vs $|\Delta_i|$ at $V_i = 0.5$ eV. The result verifies that the values of $|\Delta_i|$ in (a) are do the saddle points of the corresponding BdG condensation energy. The comparison shows that the $s_\pm$-wave Δ_8 and Δ_{10} pairings are dominant, while the $d_{x^2-y^2}$-wave Δ_9 and Δ_{11} pairings are subdominant.

trivial topological charge means that these nodal points can only mutually annihilate if their net charge vanishes.

For the A_{1g} pairing channel, we found that only 15 kinds of mean-field pairing potentials are permissible under the constraints of $p4/mmm1'$. We found that the dominant pairings are $s_\pm$-wave symmetric. The Pauli matrix structures with $\sigma_0+\sigma_z$ suggest that the pairings originate from the effectively attractive intra-orbital interactions of the electrons within the bilayer $d_{3z^2-r^2}$ orbitals. The BdG condensation energy of the dominant $s_\pm$-wave pairings is the lowest compared to any other pairing channels, as shown in Fig. 1(b). Therefore, we conclude that the A_{1g} pairing channel is the most probable one. Moreover, the subdominant pairing symmetry is $d_{x^2-y^2}$-wave symmetric. The off-diagonal matrix σ_x in the Pauli matrix structures implies that the subdominant pairings arise from the inter-orbital interactions between the $d_{3z^2-r^2}$ and $d_{x^2-y^2}$ orbitals. This result suggests a competitive relationship between the $s_\pm$- and $d_{x^2-y^2}$-wave pairings, in accordance with the results in Refs. [25, 67]. The A_{1g} pairing channel is topologically trivial, as indicated by the trivial original and refined SI groups. However, this does not necessarily imply that the system must exhibit a band gap. Accidental band nodes may still arise, and while some of these nodes can even carry topological charges, it is crucial to emphasize that not all do. In the presence of the dominant and subdominant pairings, accidental band nodes without any associated topological charges can be observed, as shown in Figs. 3 (a) and (e).

For the A_{2g} pairing channel, only 8 kinds of mean-field pairings are permissible and the dominant pairings exhibit p-wave symmetry. The Pauli matrix structures with $\sigma_0-\sigma_z$ suggest that the pairings originate from effectively attractive intra-orbital interactions between the electrons within the intra-layer $d_{x^2-y^2}$ orbitals. In this case, the topological property is also expected to be trivial, as indicated by the trivial original and refined SI groups. How-

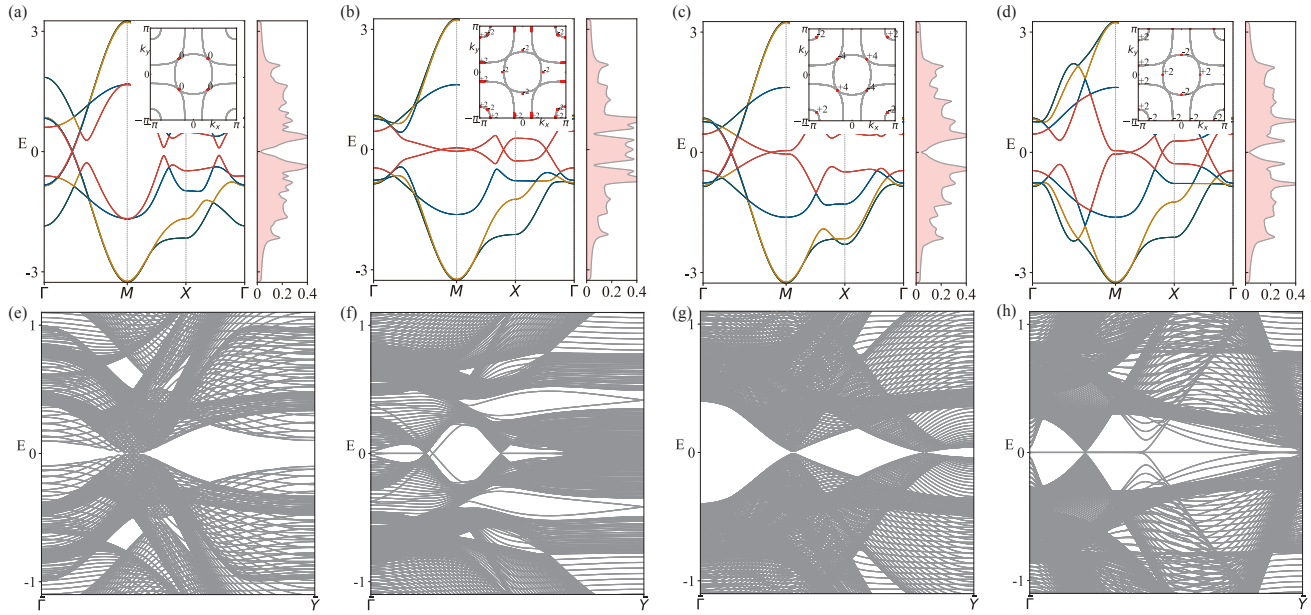

Figure 3. (a)-(d) Nodal bulk spectra of the superconducting states in the A_{1g}, A_{2g}, B_{1g}, and B_{2g} pairing channels, respectively. The subfigures display the locations of the nodal points in the BZ as well as the normalized DOSs. The numbers insight the subfigures represent the corresponding values of the winding number. (e)-(h) Corresponding edge spectra when the 2D lattice is terminated in the x direction. The parameter values employed here are list in Supplementary Notes 9-12 [56]. The figures of the band spectra are computed by the PythTB software package [66].

ever, in contrast to the A_{1g} pairing channel, termination along x or y-direction shows the coexistence of topological nodal points and the helical Majorana edge states, as shown in Figs. 3(b) and (f). This special topological state can be well indicated by the nontrivial original SIs $z_4^{\rm nodal} = -2$ and $z_4^{\rm edge} = +2$. Moreover, the projected nodal points are connected by flat Majorana edge states, analogous to the nodal points with topological edge states in zigzag ribbons of graphene. This topological feature originates from the characters $\chi_{\{2_{100}|0\}} = \chi_{\{2_{100}|0\}} = -1$, and the sign of $\tilde{\Delta}$ will be flipped under the $C_{2x(y)}$ rotation symmetries, i.e., $C_{2x(y)}\tilde{\Delta}C_{2x(y)}^T = -\tilde{\Delta}$. In the calculation of the winding number, the π_1 integral path also reverses under $C_{2x(y)}$ rotation symmetries, which implies that the winding numbers of the nodal points related by the $C_{2x(y)}$ rotation symmetries are the same. Thus the net topological charges will be preserved when the nodal points are projected onto the x or y-edges, which leads to the flat Majorana edge states. Despite the presence of the distinctive topological feature, the relatively low BdG condensation energy implies a low likelihood of its realization in experimental settings (see Supplementary Note 10 for details [56]).

For the B_{1g} pairing channel, we found only 12 kinds of mean-field pairings are permissible and the dominant pairings exhibit $d_{x^2-y^2}$-wave symmetry. The Pauli matrix structures of the dominant pairings are the same as those in the A_{1g} pairing channel. The nontrivial refined SIs $(z_{2,1}, z_{2,2}) = (1, 0)$ indicating this topological nodal superconducting phase, as illustrated in Fig. 3(c). This phase can also be indicated by the original SI $z_4 = z_4^{\rm nodal} = -2$. When the x or y-edge is terminated, the projected nodal points carry no net topological charge, and thus no flat Majorana edge states emerge in this scenario, as shown in Fig. 3(g). This nodal band structure comes from the characters $\chi_{\{2_{100}|0\}} = \chi_{\{2_{100}|0\}} = +1$, in contrast to the cases of A_{2g} and B_{2g}. Thus the B_{1g} pairing channel exhibits a remarkable characteristic: nodal points in the band structure that lack accompanying Majorana edge states (see Supplementary Note 11 for details [56]).

For B_{2g} pairing channel, we found that only 12 kinds of mean-field pairing potentials are possible. The dominant pairings are d_{xy}-wave symmetric whose Pauli matrix structures are also identical to those in the A_{1g} pairing channel. Although the refined SI group $X_{\rm BS}^{\rm BdG}$ is identical to that of the B_{1g} pairing channel, the edge spectrum under terminations along the x or y-direction exhibits nodal points accompanied by flat Majorana edge states, which has been discussed in the A_{2g} pairing channel. We can also obtain $z_4 = z_4^{\rm nodal} = -2$ and $(z_{2,1}, z_{2,2}) = (1, 0)$, which also indicates that it is a nodal TSC, as shown in Figs. 3(d) and (h). See Supplementary Note 12 for details [56].

Gapped superconducting phases.- We found that the dominant pairings in the four odd-parity channels exhibit p-wave symmetric, whose Pauli matrix structures are expressed as $\tau_y\rho_0(\sigma_0+\sigma_z)s_0$ and $\tau_x\rho_x(\sigma_0+\sigma_z)s_z$ im-

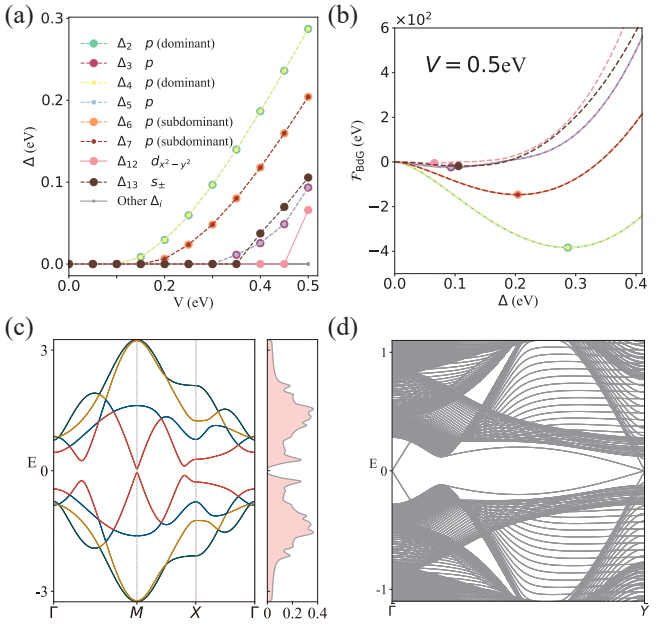

Figure 4. (a) Pairing strength Δ_i vs V_i obtained by solving the self-consistent equations in the A_{1u} pairing channel. (b) BdG condensation energy $\mathcal{F}_{\rm BdG}$ vs $|\Delta_i|$ at $V_i = 0.5$ eV. The comparison shows that the p-wave Δ_2 and Δ_4 pairings are dominant, while the p-wave Δ_6 and Δ_7 pairings are subdominant. (c) Gapped bulk spectrum. (d) Edge spectrum with helical Majorana states. The values of the pairings employed here are provided in Supplementary Note 13.

plying that they are contributed by the electrons with identical spin within the bilayer $d_{3z^2-r^2}$ orbitals. Since the odd-parity pairing channels share the same refined SI group, their topological properties are quite similar. These pairing channels would lead to the gapped topological bulk states with helical Majorana edge states. For the A_{1u}/A_{2u} channels, we found $(z_2, z_8) = (0, -3)$ and $z_4 = z_4^{\rm edge} = -3$. For the B_{1u}/B_{2u} pairing channels, we found $(z_2, z_8) = (0, 1)$ and $z_4 = z_4^{\rm edge} = +3$. Therefore, the nontrivial-valued $z_4^{\rm edge}$ denotes the mirror Chern number, corresponding to three pairs of helical Majorana edge modes in the bulk band gap, as shown in Fig. 4. Given the BdG condensation energy is slightly higher than that of the A_{1g} pairing channel, further experimental evidence is needed to determine the exact pairing symmetry.

Conclusion and Discussion.- We have studied the pairing symmetries and the corresponding topological features of $La_3Ni_2O_7$ under high pressure using BdG mean-field theory. We found that the A_{1g} pairing channel is the most probable one. The dominant pairing symmetry is $s_\pm$-wave originating from the attractive electron interaction within the bilayer $d_{3z^2-r^2}$ orbitals. We also found that the subdominant pairings exhibit $d_{x^2-y^2}$-wave symmetry, supporting the results in Refs. [25, 67]. The dominant pairing symmetries in the $A_{1g}(s_\pm)$, $B_{1g}(d_{x^2-y^2})$, and $B_{2g}(d_{xy})$ channels are in good agreement with the results of the RPA analysis presented in Ref. [43]. Furthermore, we demonstrated that dominant pairings in the A_{2g}, A_{1u}, A_{2u}, B_{1u}, and B_{2u} exhibit p-wave symmetry.

For the all of the possible pairing channels, we have comprehensively studied the relationship between pairing symmetries and topological properties using both the original and refined SI theories. We found that even-parity pairings give rise to nodal topological phases, whereas odd-parity pairings result in gapped topological phases. The distinct topological spectra thus serve as signatures of the underlying pairing symmetries. Our study provides significant insights into the superconducting pairing symmetry and mechanism of $La_3Ni_2O_7$ under high pressure.

In this work, time-reversal symmetry (TRS) is assumed to be preserved; therefore, possible TRS-breaking pairing symmetries, such as the $(d + is)$-wave pairing [29, 32], are excluded from the consideration. The origin of the effectively attractive interactions has been neglected and still requires further investigation into the underlying mechanisms. Following our discussion of the superconducting spectra, experimental techniques such as ARPES, neutron scattering, Hall effect measurements, and scanning tunneling microscopy can provide valuable insights for identifying the pairing symmetries.

We thank Zhongbo Yan and Cui-Qun Chen for helpful discussions. This work is supported by Guangdong Basic and Applied Basic Research Foundation (Grant No. 2023A1515110002, 2023A1515011796, 2024A1515011908) and the National Natural Sciences Foundation of China (Grant No. 12474247 and 92165204).

* fenggh@lingnan.edu.cn
† quanj@lingnan.edu.cn

[1] Y. Meng, Y. Yang, H. Sun, S. Zhang, J. Luo, L. Chen, X. Ma, M. Wang, F. Hong, X. Wang, and X. Yu, Density-wave-like gap evolution in $La_3Ni_2O_7$ under high pressure revealed by ultrafast optical spectroscopy, Nature Communications **15**, 10408 (2024).
[2] Z. Dong, M. Huo, J. Li, J. Li, P. Li, H. Sun, L. Gu, Y. Lu, M. Wang, Y. Wang, and Z. Chen, Visualization of oxygen vacancies and self-doped ligand holes in $La_3Ni_2O_{7-\delta}$, Nature **630**, 847 (2024).
[3] B. Chen, H. Zhang, J. Li, D. Hu, M. Huo, S. Wang, C. Xi, Z. Wang, H. Sun, M. Wang, and B. Shen, Unveiling the multiband metallic nature of the normal state in the nickelate $La_3Ni_2O_7$, Physical Review B **111**, 054519 (2025).
[4] T. Xie, M. Huo, X. Ni, F. Shen, X. Huang, H. Sun, H. C. Walker, D. Adroja, D. Yu, B. Shen, L. He, K. Cao, and M. Wang, Strong interlayer magnetic exchange coupling in $La_3Ni_2O_{7-\delta}$ revealed by inelastic neutron scattering, Science Bulletin **69**, 3221 (2024).
[5] X. Ren, R. Sutarto, X. Wu, J. Zhang, H. Huang, T. Xi-

ang, J. Hu, R. Comin, X. Zhou, and Z. Zhu, Resolving the electronic ground state of $La_3Ni_2O_{7-\delta}$ films, Communications Physics **8**, 1 (2025).

[6] D. Zhao, Y. Zhou, M. Huo, Y. Wang, L. Nie, Y. Yang, J. Ying, M. Wang, T. Wu, and X. Chen, Pressure-enhanced spin-density-wave transition in double-layer nickelate $La_3Ni_2O_{7-\delta}$, Science Bulletin 10.1016/j.scib.2025.02.019 (2025).

[7] J. Yang, H. Sun, X. Hu, Y. Xie, T. Miao, H. Luo, H. Chen, B. Liang, W. Zhu, G. Qu, C.-Q. Chen, M. Huo, Y. Huang, S. Zhang, F. Zhang, F. Yang, Z. Wang, Q. Peng, H. Mao, G. Liu, Z. Xu, T. Qian, D.-X. Yao, M. Wang, L. Zhao, and X. J. Zhou, Orbital-dependent electron correlation in double-layer nickelate $La_3Ni_2O_7$, Nature Communications **15**, 4373 (2024).

[8] M. Wang, H.-H. Wen, T. Wu, D.-X. Yao, and T. Xiang, Normal and Superconducting Properties of $La_3Ni_2O_7$, Chinese Physics Letters **41**, 077402 (2024).

[9] Z. Liu, H. Sun, M. Huo, X. Ma, Y. Ji, E. Yi, L. Li, H. Liu, J. Yu, Z. Zhang, Z. Chen, F. Liang, H. Dong, H. Guo, D. Zhong, B. Shen, S. Li, and M. Wang, Evidence for charge and spin density waves in single crystals of $La_3Ni_2O_7$ and La3Ni2O6, Science China Physics, Mechanics & Astronomy **66**, 217411 (2022).

[10] K. Chen, X. Liu, J. Jiao, M. Zou, C. Jiang, X. Li, Y. Luo, Q. Wu, N. Zhang, Y. Guo, and L. Shu, Evidence of spin density waves in $La_3Ni_2O_{7-\delta}$, Phys. Rev. Lett. **132**, 256503 (2024).

[11] S. Abadi, K.-J. Xu, E. G. Lomeli, P. Puphal, M. Isobe, Y. Zhong, A. V. Fedorov, S.-K. Mo, M. Hashimoto, D.-H. Lu, B. Moritz, B. Keimer, T. P. Devereaux, M. Hepting, and Z.-X. Shen, Electronic structure of the alternating monolayer-trilayer phase of $La_3Ni_2O_7$, Phys. Rev. Lett. **134**, 126001 (2025).

[12] H. Sun, M. Huo, X. Hu, J. Li, Z. Liu, Y. Han, L. Tang, Z. Mao, P. Yang, B. Wang, J. Cheng, D.-X. Yao, G.-M. Zhang, and M. Wang, Signatures of superconductivity near 80 K in a nickelate under high pressure, Nature **621**, 493 (2023).

[13] H. Sakakibara, M. Ochi, H. Nagata, Y. Ueki, H. Sakurai, R. Matsumoto, K. Terashima, K. Hirose, H. Ohta, M. Kato, Y. Takano, and K. Kuroki, Theoretical analysis on the possibility of superconductivity in the trilayer ruddlesden-popper nickelate $La_4Ni_3O_{10}$ under pressure and its experimental examination: Comparison with $La_3Ni_2O_7$, Phys. Rev. B **109**, 144511 (2024).

[14] M. Zhang, C. Pei, Q. Wang, Y. Zhao, C. Li, W. Cao, S. Zhu, J. Wu, and Y. Qi, Effects of pressure and doping on Ruddlesden-Popper phases Lan+1NinO3n+1, Journal of Materials Science & Technology **185**, 147 (2024).

[15] G. Wang, N. N. Wang, X. L. Shen, J. Hou, L. Ma, L. F. Shi, Z. A. Ren, Y. D. Gu, H. M. Ma, P. T. Yang, Z. Y. Liu, H. Z. Guo, J. P. Sun, G. M. Zhang, S. Calder, J.-Q. Yan, B. S. Wang, Y. Uwatoko, and J.-G. Cheng, Pressure-induced superconductivity in polycrystalline $La_3Ni_2O_{7-\delta}$, Phys. Rev. X **14**, 011040 (2024).

[16] N. Wang, G. Wang, X. Shen, J. Hou, J. Luo, X. Ma, H. Yang, L. Shi, J. Dou, J. Feng, J. Yang, Y. Shi, Z. Ren, H. Ma, P. Yang, Z. Liu, Y. Liu, H. Zhang, X. Dong, Y. Wang, K. Jiang, J. Hu, S. Nagasaki, K. Kitagawa, S. Calder, J. Yan, J. Sun, B. Wang, R. Zhou, Y. Uwatoko, and J. Cheng, Bulk high-temperature superconductivity in pressurized tetragonal $La_2PrNi_2O_7$, Nature **634**, 579 (2024).

[17] J. Li, D. Peng, P. Ma, H. Zhang, Z. Xing, X. Huang, C. Huang, M. Huo, D. Hu, Z. Dong, X. Chen, T. Xie, H. Dong, H. Sun, Q. Zeng, H.-k. Mao, and M. Wang, Identification of superconductivity in bilayer nickelate $La_3Ni_2O_7$ under high pressure up to 100 gpa, National Science Review , nwaf220 (2025).

[18] Y. Zhou, J. Guo, S. Cai, H. Sun, C. Li, J. Zhao, P. Wang, J. Han, X. Chen, Y. Chen, Q. Wu, Y. Ding, T. Xiang, H.-k. Mao, and L. Sun, Investigations of key issues on the reproducibility of high-Tc superconductivity emerging from compressed $La_3Ni_2O_7$, Matter and Radiation at Extremes **10**, 027801 (2025).

[19] J. Hou, P.-T. Yang, Z.-Y. Liu, J.-Y. Li, P.-F. Shan, L. Ma, G. Wang, N.-N. Wang, H.-Z. Guo, J.-P. Sun, Y. Uwatoko, M. Wang, G.-M. Zhang, B.-S. Wang, and J.-G. Cheng, Emergence of High-Temperature Superconducting Phase in Pressurized $La_3Ni_2O_7$ Crystals, Chinese Physics Letters **40**, 117302 (2023).

[20] Y. Zhang, D. Su, Y. Huang, Z. Shan, H. Sun, M. Huo, K. Ye, J. Zhang, Z. Yang, Y. Xu, Y. Su, R. Li, M. Smidman, M. Wang, L. Jiao, and H. Yuan, High-temperature superconductivity with zero resistance and strange-metal behaviour in $La_3Ni_2O_{7-\delta}$, Nature Physics **20**, 1269 (2024).

[21] C.-Q. Chen, Z. Luo, M. Wang, W. Wú, and D.-X. Yao, Trilayer multiorbital models of $La_4Ni_3O_{10}$, Phys. Rev. B **110**, 014503 (2024).

[22] L. Wang, Y. Li, S.-Y. Xie, F. Liu, H. Sun, C. Huang, Y. Gao, T. Nakagawa, B. Fu, B. Dong, Z. Cao, R. Yu, S. I. Kawaguchi, H. Kadobayashi, M. Wang, C. Jin, H.-k. Mao, and H. Liu, Structure Responsible for the Superconducting State in $La_3Ni_2O_7$ at High-Pressure and Low-Temperature Conditions, Journal of the American Chemical Society **146**, 7506 (2024).

[23] C. D. Ling, D. N. Argyriou, G. Wu, and J. Neumeier, Neutron Diffraction Study of $La_3Ni_2O_7$: Structural Relationships Among n=1, 2, and 3 Phases Lan+1NinO3n+1, Journal of Solid State Chemistry **152**, 517 (2000).

[24] J. Yuan, Q. Chen, K. Jiang, Z. Feng, Z. Lin, H. Yu, G. He, J. Zhang, X. Jiang, X. Zhang, Y. Shi, Y. Zhang, M. Qin, Z. G. Cheng, N. Tamura, Y.-f. Yang, T. Xiang, J. Hu, I. Takeuchi, K. Jin, and Z. Zhao, Scaling of the strange-metal scattering in unconventional superconductors, Nature **602**, 431 (2022).

[25] Q.-G. Yang, D. Wang, and Q.-H. Wang, Possible $s_{\pm}$-wave superconductivity in $La_3Ni_2O_7$, Physical Review B **108**, L140505 (2023).

[26] Y. Shen, M. Qin, and G.-M. Zhang, Effective Bi-Layer Model Hamiltonian and Density-Matrix Renormalization Group Study for the High-Tc Superconductivity in $La_3Ni_2O_7$ under High Pressure, Chinese Physics Letters **40**, 127401 (2023).

[27] Y.-f. Yang, G.-M. Zhang, and F.-C. Zhang, Interlayer valence bonds and two-component theory for high-T_c superconductivity of $La_3Ni_2O_7$ under pressure, Phys. Rev. B **108**, L201108 (2023).

[28] Y.-B. Liu, J.-W. Mei, F. Ye, W.-Q. Chen, and F. Yang, $s^{\pm}$-wave pairing and the destructive role of apical-oxygen deficiencies in $La_3Ni_2O_7$ under pressure, Phys. Rev. Lett. **131**, 236002 (2023).

[29] Z. Luo, B. Lv, M. Wang, W. Wú, and D.-X. Yao, High-T_C superconductivity in $La_3Ni_2O_7$ based on the bilayer two-orbital t-J model, npj Quantum Materials **9**, 1 (2024).

[30] Y. Gu, C. Le, Z. Yang, X. Wu, and J. Hu, Effective model

and pairing tendency in the bilayer ni-based superconductor $La_3Ni_2O_7$, Phys. Rev. B **111**, 174506 (2025).
[31] C. Xia, H. Liu, S. Zhou, and H. Chen, Sensitive dependence of pairing symmetry on Ni-eg crystal field splitting in the nickelate superconductor $La_3Ni_2O_7$, Nature Communications **16**, 1054 (2025).
[32] Z. Fan, J.-F. Zhang, B. Zhan, D. Lv, X.-Y. Jiang, B. Normand, and T. Xiang, Superconductivity in nickelate and cuprate superconductors with strong bilayer coupling, Phys. Rev. B **110**, 024514 (2024).
[33] K. Jiang, Z. Wang, and F.-C. Zhang, High-Temperature Superconductivity in $La_3Ni_2O_7$, Chinese Physics Letters **41**, 017402 (2024).
[34] Y. Wang, K. Jiang, Z. Wang, F.-C. Zhang, and J. Hu, Electronic and magnetic structures of bilayer $la_3ni_2o_7$ at ambient pressure, Phys. Rev. B **110**, 205122 (2024).
[35] Y.-H. Tian, Y. Chen, J.-M. Wang, R.-Q. He, and Z.-Y. Lu, Correlation effects and concomitant two-orbital $s_\pm$-wave superconductivity in $La_3Ni_2O_7$ under high pressure, Phys. Rev. B **109**, 165154 (2024).
[36] Y. Zhang, L.-F. Lin, A. Moreo, T. A. Maier, and E. Dagotto, Trends in electronic structures and $s_\pm$-wave pairing for the rare-earth series in bilayer nickelate superconductor $R_3Ni_2O_7$, Phys. Rev. B **108**, 165141 (2023).
[37] J. Huang, Z. D. Wang, and T. Zhou, Impurity and vortex states in the bilayer high-temperature superconductor $La_3Ni_2O_7$, Phys. Rev. B **108**, 174501 (2023).
[38] Y.-Y. Zheng and W. Wú, $s_\pm$-wave superconductivity in the bilayer two-orbital hubbard model, Phys. Rev. B **111**, 035108 (2025).
[39] X.-Z. Qu, D.-W. Qu, J. Chen, C. Wu, F. Yang, W. Li, and G. Su, Bilayer $t-J-J_\perp$ model and magnetically mediated pairing in the pressurized nickelate $La_3Ni_2O_7$, Phys. Rev. Lett. **132**, 036502 (2024).
[40] C. Lu, Z. Pan, F. Yang, and C. Wu, Interlayer-Coupling-Driven High-Temperature Superconductivity in $La_3Ni_2O_7$ under Pressure, Physical Review Letters **132**, 146002 (2024).
[41] Y. Zhang, L.-F. Lin, A. Moreo, T. A. Maier, and E. Dagotto, Structural phase transition, s±-wave pairing, and magnetic stripe order in bilayered superconductor $La_3Ni_2O_7$ under pressure, Nature Communications **15**, 2470 (2024).
[42] H. Sakakibara, N. Kitamine, M. Ochi, and K. Kuroki, Possible high T_C superconductivity in $La_3Ni_2O_7$ under high pressure through manifestation of a nearly half-filled bilayer hubbard model, Physical Review Letters **132**, 106002 (2024).
[43] F. Lechermann, J. Gondolf, S. Bötzel, and I. M. Eremin, Electronic correlations and superconducting instability in $La_3Ni_2O_7$ under high pressure, Physical Review B **108**, L201121 (2023).
[44] R. Jiang, J. Hou, Z. Fan, Z.-J. Lang, and W. Ku, Pressure driven fractionalization of ionic spins results in cuprate-like high-T_c superconductivity in $La_3Ni_2O_7$, Phys. Rev. Lett. **132**, 126503 (2024).
[45] S. Ryee, N. Witt, and T. O. Wehling, Quenched pair breaking by interlayer correlations as a key to superconductivity in $La_3Ni_2O_7$, Phys. Rev. Lett. **133**, 096002 (2024).
[46] G. Heier, K. Park, and S. Y. Savrasov, Competing d_{xy} and $s_\pm$ pairing symmetries in superconducting $La_3Ni_2O_7$: LDA + FLEX calculations, Phys. Rev. B **109**, 104508 (2024).
[47] Z. Liao, L. Chen, G. Duan, Y. Wang, C. Liu, R. Yu, and Q. Si, Electron correlations and superconductivity in $La_3Ni_2O_7$ under pressure tuning, Phys. Rev. B **108**, 214522 (2023).
[48] D. Varjas, T. O. Rosdahl, and A. R. Akhmerov, Qsymm: algorithmic symmetry finding and symmetric Hamiltonian generation, New Journal of Physics **20**, 093026 (2018).
[49] M. G. Vergniory, L. Elcoro, C. Felser, N. Regnault, B. A. Bernevig, and Z. Wang, A complete catalogue of high-quality topological materials, Nature **566**, 480 (2019).
[50] J. Cano and B. Bradlyn, Band Representations and Topological Quantum Chemistry, Annual Review of Condensed Matter Physics **12**, 225 (2021).
[51] F. Tang, H. C. Po, A. Vishwanath, and X. Wan, Comprehensive search for topological materials using symmetry indicators, Nature **566**, 486 (2019).
[52] F. Tang, H. C. Po, A. Vishwanath, and X. Wan, Efficient topological materials discovery using symmetry indicators, Nature Physics **15**, 470 (2019).
[53] B. Bradlyn, L. Elcoro, J. Cano, M. G. Vergniory, Z. Wang, C. Felser, M. I. Aroyo, and B. A. Bernevig, Topological quantum chemistry, Nature **547**, 298 (2017).
[54] F. Tang, H. C. Po, A. Vishwanath, and X. Wan, Towards ideal topological materials: Comprehensive database searches using symmetry indicators, Nature **566**, 486 (2019).
[55] L. Elcoro, B. J. Wieder, Z. Song, Y. Xu, B. Bradlyn, and B. A. Bernevig, Magnetic topological quantum chemistry, Nature Communications **12**, 5965 (2021).
[56] See Supplemental Material at [URL will be inserted by publisher] The stardard BdG Hamiltonian used in the main text; the details of the path integral formulation; the details of the original and refined SI groups and the formulas for superconductors; the comprehensive table the symmetry-allowed pairings and the details of the numerical results. The Supplemental Material also contains Refs. [17,48,50,53,55,58,60-64].
[57] Z. Luo, X. Hu, M. Wang, W. Wú, and D.-X. Yao, Bilayer two-orbital model of $La_3Ni_2O_7$ under pressure, Physical Review Letters **131**, 126001 (2023).
[58] P. Coleman, Superconductivity and BCS theory, in *Introduction to Many-Body Physics* (Cambridge University Press, 2015) p. 486–541.
[59] O. Can, T. Tummuru, R. P. Day, I. Elfimov, A. Damascelli, and M. Franz, High-temperature topological superconductivity in twisted double-layer copper oxides, Nature Physics **17**, 519 (2021).
[60] S. Ono, H. C. Po, and H. Watanabe, Refined symmetry indicators for topological superconductors in all space groups, Science Advances **6**, eaaz8367 (2020).
[61] S. Ono, Y. Yanase, and H. Watanabe, Symmetry indicators for topological superconductors, Physical Review Research **1**, 013012 (2019).
[62] S. Ono, Y. Yanase, and H. Watanabe, Symmetry indicators for topological superconductors, Phys. Rev. Res. **1**, 013012 (2019).
[63] A. Skurativska, T. Neupert, and M. H. Fischer, Atomic limit and inversion-symmetry indicators for topological superconductors, Phys. Rev. Res. **2**, 013064 (2020).
[64] T. Bzdušek and M. Sigrist, Robust doubly charged nodal lines and nodal surfaces in centrosymmetric systems, Physical Review B **96**, 155105 (2017).
[65] G.-H. Feng, Nodal higher-order topological superconduc-

tivity from C_6-symmetric dirac semimetals, Phys. Rev. B **110**, 174513 (2024).
[66] S. Coh and D. Vanderbilt, Python tight binding (pythtb) (2022).
[67] H.-X. Xu, Y. Xie, D. Guterding, and Z. Wang, Competition of superconducting pairing symmetries in $La_3Ni_2O_7$ (2025).

Supplementary Notes for "Unconventional Superconducting Pairing Symmetries in $La_3Ni_2O_7$: from the Perspective of Topology"

Guan-Hao Feng,[1,*] Jun Quan,[2,1,†] and Yusheng Hou[3]

[1] *School of Physical Science and Technology, Lingnan Normal University, Zhanjiang, 524048, China*
[2] *School of Physics, Changchun Normal University, Changchun, 130032, China*
[3] *Guangdong Provincial Key Laboratory of Magnetoelectric Physics and Devices, Center for Neutron Science and Technology, School of Physics, Sun Yat-Sen University, Guangzhou, 510275, China*

(Dated: June 3, 2025)

CONTENTS

1. STANDARD MEAN-FIELD BDG HAMILTONIAN

In this section, we provide the standard mean-field BdG Hamiltonian discussed in the main text, which is given by,

$$\mathcal{H}_{\boldsymbol{k}}^{\mathrm{BdG}} = \mathcal{H}_0 + \mathcal{H}_\Delta, \tag{1}$$

$$\mathcal{H}_0 = \begin{pmatrix} \mathcal{H}_{\boldsymbol{k}} - \mu & \\ & -\mathcal{H}_{-\boldsymbol{k}}^* + \mu \end{pmatrix}, \tag{2}$$

$$\mathcal{H}_\Delta = \begin{pmatrix} & \tilde{\Delta}_{\boldsymbol{k}} \\ \tilde{\Delta}_{\boldsymbol{k}}^\dagger & \end{pmatrix}, \tag{3}$$

where $\mathcal{H}_{\boldsymbol{k}} - \mu$ is normal-state Hamiltonian used in the main text, and $\tilde{\Delta}_{\boldsymbol{k}}$ is the pairing gap matrix. Suppose that the normal-state Hamiltonian possesses a space group symmetry G, the unitary matrix representation of a spatial symmetry $g \in G$ in the BdG Hamiltonian takes the form

$$U_{\boldsymbol{k}}^{\mathrm{BdG}}(g) \equiv \begin{pmatrix} U_{\boldsymbol{k}}(g) & \\ & \chi_g U_{-\boldsymbol{k}}^*(g) \end{pmatrix}. \tag{4}$$

Here, $U_{\boldsymbol{k}}(g)$ acts on the normal-state Hamiltonian, and the phase $\chi_g \in U(1)$ characterizes the symmetry property of $\tilde{\Delta}_{\boldsymbol{k}}$. Under the action of g, the pairing gap matrix transforms as $U_{\boldsymbol{k}}(g)\tilde{\Delta}_{\boldsymbol{k}}U_{-\boldsymbol{k}}(g)^T = \chi_g\tilde{\Delta}_{g\boldsymbol{k}}$. When the time-reversal symmetry is preserved, χ_g must be either ± 1 [1–3]. If the BdG Hamiltonian respects the symmetries of the point group $4/mmm$ (D_{4h}), the phase χ_g is the character of $4/mmm$ and the pairings must belong to one of the 1D pairing channels. The BdG time-reversal symmetry takes a block-diagonal form

$$U_{\mathcal{T}}^{\mathrm{BdG}} = \begin{pmatrix} U_{\mathcal{T}} & \\ & U_{\mathcal{T}}^* \end{pmatrix}. \tag{5}$$

The particle-hole symmetry takes a block off-diagonal form [3]

$$U_{\mathcal{P}}^{\mathrm{BdG}} = \begin{pmatrix} & \xi\mathbb{1} \\ +\mathbb{1} & \end{pmatrix}, \tag{6}$$

where $\xi = \pm 1$ depends on the physical realization of the superconductor ($\left(U_{\mathcal{P}}^{\mathrm{BdG}}\right)^2 = \xi$). The matrix representations of the generators of the BdG Hamiltonian can be constructed from those of the normal-state Hamiltonian. Furthermore, by using the Qsymm software package [4], all symmetry-allowed pairing gap matrices can be identified. The generators of normal-state Hamiltonian of Eq. 1 in the main text can be obtain by MagneticTB software package [5], which are given by

$$\{4_{001}|0\} = \begin{pmatrix} e^{-\frac{i\pi}{4}} & 0 & 0 & 0 & 0 & 0 & 0 & 0 \\ 0 & e^{\frac{i\pi}{4}} & 0 & 0 & 0 & 0 & 0 & 0 \\ 0 & 0 & e^{\frac{3i\pi}{4}} & 0 & 0 & 0 & 0 & 0 \\ 0 & 0 & 0 & e^{-\frac{3i\pi}{4}} & 0 & 0 & 1 & 0 \\ 0 & 0 & 0 & 0 & e^{-\frac{i\pi}{4}} & 0 & 0 & 0 \\ 1 & 0 & 0 & 0 & 0 & e^{\frac{i\pi}{4}} & 0 & 0 \\ 0 & 0 & 0 & 0 & 0 & 0 & e^{\frac{3i\pi}{4}} & 0 \\ 0 & 0 & 1 & 0 & 0 & 0 & 0 & e^{-\frac{3i\pi}{4}} \end{pmatrix}, \tag{7}$$

$$\{2_{100}|0\} = \begin{pmatrix} 0 & 0 & 0 & 0 & 0 & -i & 0 & 0 \\ 0 & 0 & 0 & 0 & -i & 0 & 0 & 0 \\ 0 & 0 & 0 & 0 & 0 & 0 & 0 & -i \\ 0 & 0 & 0 & 0 & 0 & 0 & -i & 0 \\ 0 & -i & 0 & 0 & 0 & 0 & 0 & 0 \\ -i & 0 & 0 & 0 & 0 & 0 & 0 & 0 \\ 0 & 0 & 0 & -i & 0 & 0 & 0 & 0 \\ 0 & 0 & -i & 0 & 0 & 0 & 0 & 0 \end{pmatrix}, \tag{8}$$

$$\{2_{010}|0\} = \begin{pmatrix} 0 & 0 & 0 & 0 & 0 & -1 & 0 & 0 \\ 0 & 0 & 0 & 0 & 1 & 0 & 0 & 0 \\ 0 & 0 & 0 & 0 & 0 & 0 & 0 & -1 \\ 0 & 0 & 0 & 0 & 0 & 0 & 1 & 0 \\ 0 & -1 & 0 & 0 & 0 & 0 & 0 & 0 \\ 1 & 0 & 0 & 0 & 0 & 0 & 0 & 0 \\ 0 & 0 & 0 & -1 & 0 & 0 & 0 & 0 \\ 0 & 0 & 1 & 0 & 0 & 0 & 0 & 0 \end{pmatrix}, \tag{9}$$

$$\{2_{-110}|0\} = \begin{pmatrix} 0 & 0 & 0 & 0 & 0 & -e^{\frac{i\pi}{4}} & 0 & 0 \\ 0 & 0 & 0 & 0 & -e^{\frac{3i\pi}{4}} & 0 & 0 & 0 \\ 0 & 0 & 0 & 0 & 0 & 0 & 0 & e^{\frac{i\pi}{4}} \\ 0 & 0 & 0 & 0 & 0 & 0 & e^{\frac{3i\pi}{4}} & 0 \\ 0 & -e^{\frac{i\pi}{4}} & 0 & 0 & 0 & 0 & 0 & 0 \\ -e^{\frac{3i\pi}{4}} & 0 & 0 & 0 & 0 & 0 & 0 & 0 \\ 0 & 0 & 0 & e^{\frac{i\pi}{4}} & 0 & 0 & 0 & 0 \\ 0 & 0 & e^{\frac{3i\pi}{4}} & 0 & 0 & 0 & 0 & 0 \end{pmatrix}, \tag{10}$$

$$\{-1|0\} = \begin{pmatrix} 0 & 0 & 0 & 0 & 1 & 0 & 0 & 0 \\ 0 & 0 & 0 & 0 & 0 & 1 & 0 & 0 \\ 0 & 0 & 0 & 0 & 0 & 0 & 1 & 0 \\ 0 & 0 & 0 & 0 & 0 & 0 & 0 & 1 \\ 1 & 0 & 0 & 0 & 0 & 0 & 0 & 0 \\ 0 & 1 & 0 & 0 & 0 & 0 & 0 & 0 \\ 0 & 0 & 1 & 0 & 0 & 0 & 0 & 0 \\ 0 & 0 & 0 & 1 & 0 & 0 & 0 & 0 \end{pmatrix}, \tag{11}$$

$$\{1'|0\} = \begin{pmatrix} 0 & 1 & 0 & 0 & 0 & 0 & 0 & 0 \\ -1 & 0 & 0 & 0 & 0 & 0 & 0 & 0 \\ 0 & 0 & 0 & 1 & 0 & 0 & 0 & 0 \\ 0 & 0 & -1 & 0 & 0 & 0 & 0 & 0 \\ 0 & 0 & 0 & 0 & 0 & 1 & 0 & 0 \\ 0 & 0 & 0 & 0 & -1 & 0 & 0 & 0 \\ 0 & 0 & 0 & 0 & 0 & 0 & 0 & 1 \\ 0 & 0 & 0 & 0 & 0 & 0 & -1 & 0 \end{pmatrix} \mathcal{K}. \tag{12}$$

2. PATH INTEGRAL FORMULATION

In this section, we review the path integral formulation of BCS theory [6] and derive the self-consistent gap equation and free energy for the multi-orbital case. We begin with the extended multi-orbital attractive Hubbard interactions of Eq. (2) in the main text,

$$H_{\rm attr} = -\frac{1}{N}\sum_{kk'\alpha\beta ss'} V_{\alpha\beta ss'} e^{-i(k-k')\cdot r_{\alpha\beta}} c^\dagger_{k\alpha s} c^\dagger_{-k\beta s'} c_{-k'\beta s'} c_{k'\alpha s}. \tag{13}$$

These attractive interactions are nonlocal since an exponential factor $e^{-i(k-k')\cdot r_{\alpha\beta}}$ occurs, which leads to the non-local superconducting pairings such as the $s_\pm$-, $p_x \pm ip_y$-, $d_{x^2-y^2}$-, and d_{xy}- wave superconducting pairings. The standard mean-field approximation gives: $b_{k'\alpha\beta ss'} = \langle c_{-k'\beta s'} c_{k'\alpha s}\rangle$ and $b^\dagger_{k\alpha\beta ss'} = \left\langle c^\dagger_{k\alpha s} c^\dagger_{-k\beta s'}\right\rangle$. By performing the substitution:

$$c^\dagger_{k\alpha s} c^\dagger_{-k\beta s'} = b^\dagger_k + \left(c^\dagger_{k\alpha s} c^\dagger_{-k\beta s'} - b^\dagger_k\right), \tag{14}$$

$$c_{-k'\beta s'} c_{k'\alpha s} = b_{k'} + \left(c_{-k'\beta s'} c_{k'\alpha s} - b_{k'}\right), \tag{15}$$

and defining $\Delta_{\alpha\beta ss'} = -\frac{1}{N}\sum_{k'} V_{\alpha\beta ss'} e^{+ik'\cdot r_{\alpha\beta}} b_{k'\alpha\beta ss'}$ and $\Delta^*_{\alpha\beta ss'} = -\frac{1}{N}\sum_k V_{\alpha\beta ss'} e^{-ik\cdot r_{\alpha\beta}} b^\dagger_{k\alpha\beta ss'}$, we can obtain

$$\begin{aligned}
H_{\rm attr} &= -\frac{1}{N}\sum_{kk'\alpha\beta ss'} V_{\alpha\beta ss'} e^{-i(k-k')\cdot r_{\alpha\beta}} \left[b^\dagger_{k\alpha\beta ss'} + \left(c^\dagger_{k\alpha s} c^\dagger_{-k\beta s'} - b^\dagger_{k\alpha\beta ss'}\right)\right]\left[b_{k'\alpha\beta ss'} + (c_{-k'\beta s'} c_{k'\alpha s} - b_{k'\alpha\beta ss'})\right] \\
&\approx -\frac{1}{N}\sum_{kk'\alpha\beta ss'} V_{\alpha\beta ss'} e^{-i(k-k')\cdot r_{\alpha\beta}} \left[b^\dagger_{k\alpha\beta ss'}\left(c_{-k'\beta s'} c_{k'\alpha s} - b_{k'\alpha\beta ss'}\right) + b_{k'\alpha\beta ss'}\left(c^\dagger_{k\alpha s} c^\dagger_{-k\beta s'} - b^\dagger_{k\alpha\beta ss'}\right) + b^\dagger_{k\alpha\beta ss'} b_{k'\alpha\beta ss'}\right] \\
&= \sum_{k\alpha\beta ss'}\left(\Delta^*_{\alpha\beta ss'} e^{ik\cdot r_{\alpha\beta}} c_{-k\beta s'} c_{k\alpha s} + \Delta_{\alpha\beta ss'} e^{-ik\cdot r_{\alpha\beta}} c^\dagger_{k\alpha s} c^\dagger_{-k\beta s'}\right) + \sum_{\alpha\beta ss'} \frac{N}{V_{\alpha\beta ss'}} \Delta^*_{\alpha\beta ss'}\Delta_{\alpha\beta ss'} \\
&= H_\Delta + \sum_{\alpha\beta ss'} \frac{N}{V_{\alpha\beta ss'}} \Delta^*_{\alpha\beta ss'}\Delta_{\alpha\beta ss'}
\end{aligned} \tag{16}$$

By using the Nambu spinor $\psi^\dagger_k = \left(c^\dagger_k, c_k\right)$, we can write the pairing Hamiltonian in a compact form:

$$H_\Delta = \sum_k \left(\psi_k \tilde{\Delta}^\dagger_k \psi_k + \psi^\dagger_k \tilde{\Delta}_k \psi^\dagger_k\right) + \sum_{\alpha\beta ss'} \frac{N}{V_{\alpha\beta ss'}} \Delta^*_{\alpha\beta ss'}\Delta_{\alpha\beta ss'} \tag{17}$$

The partition function and the action are given by

$$Z_{\rm BCS} = \int D[\bar{\Delta}, \Delta, \bar{\psi}, \psi] e^{-S} \tag{18}$$

$$S = \int_0^\beta d\tau \left\{\sum_k \bar{\psi}_k \left(\partial_\tau + \mathcal{H}^{\rm BdG}_k\right)\psi_k + \sum_{\alpha\beta ss'} \frac{N}{V_{\alpha\beta ss'}} \bar{\Delta}_{\alpha\beta ss'}\Delta_{\alpha\beta ss'}\right\}. \tag{19}$$

Since the action S is explicitly quadratic in the Fermi fields, we can carry out the Gaussian integral of the Fermi fields to obtain

$$Z_{\rm BCS} = \int D[\bar{\Delta}, \Delta] e^{-S_E[\bar{\Delta},\Delta]} \tag{20}$$

$$e^{-S_E[\bar{\Delta},\Delta]} = \prod_k \det\left[\partial_\tau + \mathcal{H}^{\rm BdG}_k\right] e^{-\int_0^\beta d\tau \sum_{\alpha\beta ss'} \frac{N}{V_{\alpha\beta ss'}} \bar{\Delta}_{\alpha\beta ss'}\Delta_{\alpha\beta ss'}}. \tag{21}$$

Then the effective action is given by

$$S_E\left[\bar{\Delta},\Delta\right]=\sum_{\alpha\beta ss'}\frac{\beta N}{V_{\alpha\beta ss'}}\bar{\Delta}_{\alpha\beta ss'}\Delta_{\alpha\beta ss'}-\int_0^\beta d\tau\sum_k\mathrm{Tr}\left[\ln\left(\partial_\tau+\mathcal{H}_k^{\mathrm{BdG}}\right)\right], \tag{22}$$

where we have replaced $\ln\det\to\mathrm{Tr}\ln$. Then we take $\partial_\tau+\mathcal{H}_k^{\mathrm{BdG}}\to[-i\omega_n+\mathcal{H}_k^{\mathrm{BdG}}]$ to obtain

$$\begin{aligned}S_E\left[\bar{\Delta},\Delta\right]&=\sum_{\alpha\beta ss'}\frac{\beta N}{V_{\alpha\beta ss'}}\Delta^*_{\alpha\beta ss'}\Delta_{\alpha\beta ss'}-\sum_{kn}\mathrm{Tr}\left[\ln\left(-i\omega_n+\mathcal{H}_k^{\mathrm{BdG}}\right)\right]\\&=\sum_{\alpha\beta ss'}\frac{\beta N}{V_{\alpha\beta ss'}}\Delta^*_{\alpha\beta ss'}\Delta_{\alpha\beta ss'}-\sum_{kn}\mathrm{Tr}\left[\ln\left(-g^{-1}(k,i\omega_n)\right)\right].\end{aligned} \tag{23}$$

To evaluate the saddle-point condition for this effective action, we minimize the effective action by requiring that $\partial S_E/\partial\bar{\Delta}_{\alpha\beta ss'k}=0$. This yields:

$$\sum_{\alpha\beta ss'}\frac{\beta N}{V_{\alpha\beta ss'}}\Delta_{\alpha\beta ss'}=\frac{\partial\sum_{kn}\mathrm{Tr}\left[\ln\left(-g^{-1}(k,i\omega_n)\right)\right]}{\partial\Delta^*_{\alpha\beta ss'}}. \tag{24}$$

For a specified kind i of the superconducting pairings, $\Delta_{\alpha\beta ss'}=\Delta_i$ and $V_{\alpha\beta ss'}=V_i$, the complex order parameters satisfy the self-consistent equation:

$$\frac{\beta Nn}{V_i}\Delta_i=\frac{\partial\sum_{kn}\mathrm{Tr}\left[\ln\left(-g^{-1}(k,i\omega_n)\right)\right]}{\partial\Delta_i^*}. \tag{25}$$

By using the identity $\partial_\Delta\left(\mathrm{Tr}\ln A\right)=\mathrm{Tr}\left[\partial_\Delta AA^{-1}\right]$, this simplifies to

$$\frac{\beta Nn}{V_i}\Delta_i=\sum_{kn}\mathrm{Tr}\left[\frac{\partial\mathcal{H}_k^{\mathrm{BdG}}}{\partial\Delta_i}g(k,i\omega_n)\right]. \tag{26}$$

For a function $F(z)$ satisfing $F(z^*)=-F^*(z)$, the sum of the imaginary frequency is calculated by

$$\begin{aligned}\sum_n F(i\omega_n)&=\oint_{\mathrm{Im\,axis}}\frac{dz}{2\pi i}\beta n_F(z)F(z)\\&=\oint_{\mathrm{Real\,axis}}\frac{dz}{2\pi i}\beta n_F(z)F(z)\\&=\int_{-\infty}^{+\infty}\left[\frac{d\omega}{2\pi i}\beta n_F(\omega)F(z)\right]_{z=\omega-i\delta}-\int_{-\infty}^{+\infty}\left[\frac{d\omega}{2\pi i}\beta n_F(\omega)F(z)\right]_{z=\omega+i\delta}\\&=\int_{-\infty}^{+\infty}\frac{d\omega}{\pi}\beta n_F(\omega)\mathrm{Im}\left(F(z)\right)_{z=\omega-i\delta}.\end{aligned} \tag{27}$$

The Matsubara Green function can be written as

$$\begin{aligned}g(k,i\omega_n)&=\left(i\omega_n-\mathcal{H}_k^{\mathrm{BdG}}\right)^{-1}\\&=U_kU_k^\dagger\left(i\omega_n-\mathcal{H}_k^{\mathrm{BdG}}\right)^{-1}U_kU_k^\dagger\\&=U_k\left(U_k^\dagger\left(i\omega_n-\mathcal{H}_k^{\mathrm{BdG}}\right)U_k\right)^{-1}U_k^\dagger\\&=U_k\left(i\omega_n-E_k^{\mathrm{BdG}}\right)^{-1}U_k^\dagger.\end{aligned} \tag{28}$$

Thus

$$\sum_{kn}\mathrm{Tr}\left[\frac{\partial\mathcal{H}_k^{\mathrm{BdG}}}{\partial\Delta_i}g(k,i\omega_n)\right]=\sum_k\mathrm{Tr}\left[\int_{-\infty}^{+\infty}\frac{d\omega}{\pi}\beta n_F(\omega)\mathrm{Im}\left(\frac{\partial\mathcal{H}_k^{\mathrm{BdG}}}{\partial\Delta_i}g(k,z)\right)_{z=\omega-i\delta}\right]$$
$$=\sum_k\mathrm{Tr}\left[\int_{-\infty}^{+\infty}d\omega\beta n_F(\omega)\frac{\partial\mathcal{H}_k^{\mathrm{BdG}}}{\partial\Delta_i}U_k\delta(\omega-E_k^{\mathrm{BdG}})U_k^\dagger\right]$$
$$=\sum_k\mathrm{Tr}\left[\beta\frac{\partial\mathcal{H}_k^{\mathrm{BdG}}}{\partial\Delta_i}U_k n_F(E_k^{\mathrm{BdG}})U_k^\dagger\right]. \tag{29}$$

Then we can obtain the self-consistent gap equation Eq. (6) in the main text

$$\Delta_i=-\frac{V_i}{Nn}\sum_k\mathrm{Tr}\left[\frac{\partial\mathcal{H}_k^{\mathrm{BdG}}}{\partial\Delta_i}U_k n_F(E_k^{\mathrm{BdG}})U_k^\dagger\right], \tag{30}$$

where n is the number of the non-zero elements in the specified pairing matrix H_Δ. The free energy is given by

$$\begin{aligned}
\mathcal{F}=\frac{S_E}{\beta}&=\sum_{\alpha\beta ss'}\frac{N}{V_{\alpha\beta ss'}}\Delta^*_{\alpha\beta ss'}\Delta_{\alpha\beta ss'}-k_BT\sum_{kn}\mathrm{Tr}\left[\ln\left(-i\omega_n+\mathcal{H}_k^{\mathrm{BdG}}\right)\right]\\
&=\frac{Nn}{V_i}\left|\Delta_i\right|^2-k_BT\sum_{kn}\ln\det\left[-i\omega_n+\mathcal{H}_k^{\mathrm{BdG}}\right]\\
&=\frac{Nn}{V_i}\left|\Delta_i\right|^2-k_BT\sum_{k\alpha n}\left[\ln(-i\omega_n+E_{k\alpha}^{\mathrm{BdG}})+\ln(-i\omega_n-E_{k\alpha}^{\mathrm{BdG}})\right]\\
&=\frac{Nn}{V_i}\left|\Delta_i\right|^2-k_BT\sum_{k\alpha}\int_{-\infty}^{+\infty}\frac{d\omega}{\pi}\beta n_F(\omega)\left(\mathrm{Im}\left(\ln(E_{k\alpha}^{\mathrm{BdG}}-\omega)\right)_{z=\omega-i\delta}+\mathrm{Im}\left(\ln(-E_{k\alpha}^{\mathrm{BdG}}-\omega)\right)_{z=\omega-i\delta}\right)\\
&=\frac{Nn}{V_i}\left|\Delta_i\right|^2-\left(k_BT\sum_{k\alpha}\int_{E_{k\alpha}^{\mathrm{BdG}}}^{+\infty}d\omega\beta n_F(\omega)+k_BT\sum_{k\alpha}\int_{-E_{k\alpha}^{\mathrm{BdG}}}^{+\infty}d\omega\beta n_F(\omega)\right)\\
&=\frac{Nn}{V_i}\left|\Delta_i\right|^2-k_BT\sum_{k\alpha}\left[\ln\left[1+e^{-\beta E_{k\alpha}^{\mathrm{BdG}}}\right]+\ln\left[1+e^{\beta E_{k\alpha}^{\mathrm{BdG}}}\right]\right]\\
&=\frac{Nn}{V_i}\left|\Delta_i\right|^2-2k_BT\sum_{k\alpha}\ln\left[2\cosh(\beta E_{k\alpha}^{\mathrm{BdG}}/2)\right].
\end{aligned} \tag{31}$$

3. SUMMARY OF THE TOPOLOGICAL CLASSIFICATION AND WINDING NUMBER ALGORITHM

In this section, we present a summary of the topological classification discussed in the main text. We also outline the winding number algorithm employed for numerical calculations. The main results of the topological analysis are summarized in Table I.

TABLE I. Summary of the topological analysis. The first six columns list the character table of the points group $4/mmm(D_{4h})$. The seventh and eighth columns list the original SI group and the refined SI group, respectively. The ninth to twelfth columns present the AZ+I classification together with the Cartan label (CL). The last two columns list the corresponding homotopy groups and topological charge, respectively, which is adopt from Tab. 1 in Ref. [7].

$4/mmm(D_{4h})$	$\chi_{\{-1\|0\}}$	$\chi_{\{2_{100}\|0\}}$	$\chi_{\{2_{010}\|0\}}$	$\chi_{\{2_{110}\|0\}}$	$\chi_{\{4_{001}\|0\}}$	$X_{\rm BS}$	$X_{\rm BS}^{\rm BdG}$	$\mathfrak{T}^2$	$\mathfrak{P}^2$	$\mathcal{C}^2$	CL	$\pi_{p=1}(M_{\rm CL})$	$c_{\rm CL}(S_{p=1})$
A_{1g}	1	1	1	1	1	$\mathbb{Z}_4$	-	-1	1	1	DIII	$2\mathbb{Z}$	$\int q^{-1}dq$
A_{2g}	1	-1	-1	-1	1		$\mathbb{Z}_2\times\mathbb{Z}_2$						
B_{1g}	1	1	1	-1	-1								
B_{2g}	1	-1	-1	1	-1								
A_{1u}	-1	1	1	1	1		$\mathbb{Z}_2\times\mathbb{Z}_8$	-1	-1	1	CII	0	-
A_{2u}	-1	-1	-1	-1	1		$\mathbb{Z}_2\times\mathbb{Z}_8$						
B_{1u}	-1	1	1	-1	-1								
B_{2u}	-1	-1	-1	1	-1								

In the presence of the chiral symmetry $\mathcal{C}=\mathcal{T}\mathcal{P}$, the generic BdG Hamiltonian can always be unitarily transformed into an off-diagonal form by

$$\begin{aligned}\tilde{H}_{\rm BdG}(k) &= V H_{\rm BdG}(k) V^\dagger \\ &= V\begin{pmatrix} H_k-\mu & \Delta_k \\ \Delta_k^\dagger & -H_{-k}^*+\mu \end{pmatrix} V^\dagger \\ &= \begin{pmatrix} & H_k-\mu+i\mathcal{T}\Delta_k^\dagger \\ H_k-\mu-i\mathcal{T}\Delta_k^\dagger & \end{pmatrix},\end{aligned} \tag{32}$$

where

$$V=\frac{1}{\sqrt{2}}\begin{pmatrix} \mathbb{I} & i\mathcal{T} \\ \mathbb{I} & -i\mathcal{T}\end{pmatrix}. \tag{33}$$

The matrix $H_k-\mu+i\mathcal{T}\Delta_k^\dagger$ is generically non-Hermitian and can be decomposed by singular value decomposition (SVD) as $H_k-\mu+i\mathcal{T}\Delta_k^\dagger=U_k^\dagger D_k V_k$, with U_k and V_k being the unitary matrices and D_k being the diagonal matrix. The matrix elements of D_k are the positive eigenvalues of $H_{\rm BdG}(k)$ and can be adiabatically deformed into the identity matrix $\mathbb{I}$ without closing the energy gap at momentum k. This deformation also deforms $H_k-\mu+i\mathcal{T}\Delta_k^\dagger$ into a unitary matrix $Q_k=U_k^\dagger V_k$. So the winding number of Q_k along an arbitrary closed path S^1 around a nodal point is defined as

$$\pi_1(M_{\rm DIII})=\frac{i}{2\pi}\oint_{S^1} dk\cdot{\rm Tr}\left[Q_k^\dagger\nabla_k Q_k\right]\in\mathbb{Z}. \tag{34}$$

4. DOUBLE SI GROUP IN TYPE-II DOUBLE LG $p4/mmm1'$

In this section, we calculate the original double SI group in Type-II Double LG $p4/mmm1'$. Following the theory of SI [8–11], for Type-II LG $p4/mmm1'$, the symmetry data vector $\boldsymbol{B}$ that satisfies the compatibility relations is given by $\boldsymbol{B} = \big(m(\bar{\Gamma}_6), m(\bar{\Gamma}_7), m(\bar{\Gamma}_8), m(\bar{\Gamma}_9), m(\bar{M}_6), m(\bar{M}_7), m(\bar{M}_8), m(\bar{M}_9), m(\bar{X}_5), m(\bar{X}_6)\big)^T$, where $m(u_k^\alpha)$ are the multiplicities of the small irreps u_k^α of the little group at the high-symmetry momentums Γ, M, and X. The EBR matrix in basics $\Big(\boldsymbol{B}^{(\bar{E}_{2g})_{1a}}, \boldsymbol{B}^{(\bar{E}_{1g})_{1a}}, \boldsymbol{B}^{(\bar{E}_{2u})_{1a}}, \boldsymbol{B}^{(\bar{E}_{1u})_{1a}}, \boldsymbol{B}^{(\bar{E}_{2g})_{1b}}, \boldsymbol{B}^{(\bar{E}_{1g})_{1b}}, \boldsymbol{B}^{(\bar{E}_{2u})_{1b}}, \boldsymbol{B}^{(\bar{E}_{1u})_{1b}}, \boldsymbol{B}^{(\bar{E}_{g})_{2c}}, \boldsymbol{B}^{(\bar{E}_{u})_{2c}}\Big)$ is then given by [12, 13]

$$\mathcal{EBR} = \begin{pmatrix} 1&0&0&0&1&0&0&0&1&0\\ 0&1&0&0&0&1&0&0&1&0\\ 0&0&1&0&0&0&1&0&0&1\\ 0&0&0&1&0&0&0&1&0&1\\ 1&0&0&0&0&1&0&0&0&1\\ 0&1&0&0&1&0&0&0&0&1\\ 0&0&1&0&0&0&0&1&1&0\\ 0&0&0&1&0&0&1&0&1&0\\ 1&1&0&0&0&0&1&1&1&1\\ 0&0&1&1&1&1&0&0&1&1 \end{pmatrix}. \tag{35}$$

The EBR matrix admits a Smith normal decomposition:

$$L^{-1}_{\mathcal{EBR}} = \begin{pmatrix} 0&0&0&0&1&0&0&0&0&0\\ 0&1&0&0&0&0&0&0&0&0\\ 0&0&0&0&0&0&1&0&0&0\\ 0&0&0&1&0&0&0&0&0&0\\ 1&1&1&0&0&0&-1&0&-1&0\\ 0&1&0&-1&1&0&0&1&-1&0\\ 0&0&0&-1&0&0&0&1&0&0\\ 0&-2&-1&1&-2&0&1&-1&2&0\\ -1&-1&-1&-1&1&1&1&1&0&0\\ -1&-1&-1&-1&0&0&0&0&1&1 \end{pmatrix}, \tag{36}$$

$$\Lambda_{\mathcal{EBR}} = \begin{pmatrix} 1&0&0&0&0&0&0&0&0&0\\ 0&1&0&0&0&0&0&0&0&0\\ 0&0&1&0&0&0&0&0&0&0\\ 0&0&0&1&0&0&0&0&0&0\\ 0&0&0&0&1&0&0&0&0&0\\ 0&0&0&0&0&1&0&0&0&0\\ 0&0&0&0&0&0&1&0&0&0\\ 0&0&0&0&0&0&0&4&0&0\\ 0&0&0&0&0&0&0&0&0&0\\ 0&0&0&0&0&0&0&0&0&0 \end{pmatrix}, \tag{37}$$

$$R^{-1}_{\mathcal{EBR}} = \begin{pmatrix} 1&0&0&0&0&0&0&1&-1&-1\\ 0&1&0&0&0&-1&0&-1&-1&-1\\ 0&0&1&0&0&-1&0&-2&-1&-1\\ 0&0&0&1&0&0&0&0&-1&-1\\ 0&0&0&0&1&0&0&1&1&0\\ 0&0&0&0&0&0&0&-1&1&0\\ 0&0&0&0&0&-1&1&-2&1&0\\ 0&0&0&0&0&0&0&0&1&0\\ 0&0&0&0&0&1&0&2&0&1\\ 0&0&0&0&0&0&0&0&0&1 \end{pmatrix}. \tag{38}$$

Thus, the double SI group of Type-II SLG $p4/mmm1'$ is $X_{\rm BS} = \mathbb{Z}_4$ and given by

$$z_4 = -2m(\bar{\Gamma}_7) - m(\bar{\Gamma}_8) + m(\bar{\Gamma}_9) - 2m(\bar{M}_6) + m(\bar{M}_8) - m(\bar{M}_9) + m(\bar{X}_5) \mod 4. \tag{39}$$

5. REFINED SI GROUP FOR THE B_{1g} AND B_{2g} SUPERCONDUCTING PAIRING CHANNELS

For the B_{1g} and B_{2g} superconducting pairing channel, we can use the refined double SI to indicate the topological superconducting property [3]. The symmetry data vector is given by $\boldsymbol{B}^{\mathrm{BdG}} = \boldsymbol{B} - \boldsymbol{B}^{\mathrm{vac}}$, with $\boldsymbol{B}^{\mathrm{vac}} = (2,2,0,0,2,2,0,0,4,0)$. In this pairing channel, the refined EBR matrix is given by $\{\mathcal{EBR}\}^{\mathrm{BdG}} = \mathcal{EBR} - \overline{\mathcal{EBR}}$, with

$$\overline{\mathcal{EBR}} = \begin{pmatrix} 0&1&0&0&0&1&0&0&1&0\\ 1&0&0&0&1&0&0&0&1&0\\ 0&0&0&1&0&0&0&1&0&1\\ 0&0&1&0&0&0&1&0&0&1\\ 0&1&0&0&1&0&0&0&0&1\\ 1&0&0&0&0&1&0&1&0&1\\ 0&0&0&1&0&0&1&0&1&0\\ 0&0&1&0&0&0&0&0&1&0\\ 1&1&0&0&0&0&1&1&1&1\\ 0&0&1&1&1&1&0&0&1&1 \end{pmatrix}. \tag{40}$$

Such that the refined EBR matrix also admits the Smith normal decomposition:

$$\left(L^{\mathrm{BdG}}_{\mathcal{EBR}}\right)^{-1} = \begin{pmatrix} 1&0&0&0&0&0&0&0&0&0\\ 0&0&0&-1&-1&-1&0&0&0&0\\ 0&0&0&0&-1&-1&0&0&0&0\\ -1&0&0&-1&0&-1&0&1&0&0\\ -1&0&0&0&-1&-2&0&0&0&0\\ 0&0&1&1&0&0&0&0&0&0\\ 0&0&0&0&1&1&1&1&0&0\\ 1&1&0&0&0&0&0&0&0&0\\ 0&0&0&0&0&0&0&0&1&0\\ 0&0&0&0&0&0&0&0&0&1 \end{pmatrix}, \tag{41}$$

$$\Lambda^{\mathrm{BdG}}_{\mathcal{EBR}} = \begin{pmatrix} 1&0&0&0&0&0&0&0&0&0\\ 0&1&0&0&0&0&0&0&0&0\\ 0&0&1&0&0&0&0&0&0&0\\ 0&0&0&2&0&0&0&0&0&0\\ 0&0&0&0&2&0&0&0&0&0\\ 0&0&0&0&0&0&0&0&0&0\\ 0&0&0&0&0&0&0&0&0&0\\ 0&0&0&0&0&0&0&0&0&0\\ 0&0&0&0&0&0&0&0&0&0\\ 0&0&0&0&0&0&0&0&0&0 \end{pmatrix}, \tag{42}$$

$$\left(R^{\mathrm{BdG}}_{\mathcal{EBR}}\right)^{-1} = \begin{pmatrix} 1&0&0&0&0&0&0&1&0&0\\ 0&0&1&0&-1&0&0&1&0&0\\ 0&1&0&-1&0&0&1&0&0&0\\ 0&0&1&0&-1&0&1&0&0&0\\ 0&0&2&0&-2&1&0&0&0&0\\ 0&0&1&0&-1&1&0&0&0&0\\ 0&0&1&1&-1&0&0&0&0&0\\ 0&0&1&0&0&0&0&0&0&0\\ 0&0&1&0&-1&0&0&0&1&0\\ 0&0&1&0&-1&0&0&0&0&1 \end{pmatrix}. \tag{43}$$

The double SI group of the superconducting states respecting Type-II SLG $p4/mmm1'$ in the B_{1g} and B_{2g} pairing channels is $X^{\mathrm{BdG}}_{\mathrm{BS}} = \mathbb{Z}_2 \times \mathbb{Z}_2$ and given by

$$z_2 = -m(\bar{\Gamma}_6) - m(\bar{\Gamma}_9) - m(\bar{M}_7) + m(\bar{M}_9) \mod 2 \tag{44}$$

$$z_2 = -m(\bar{\Gamma}_6) - m(\bar{M}_6) - 2m(\bar{M}_7) \mod 2 \tag{45}$$

6. REFINED SI GROUP FOR THE A_{1u} AND A_{2u} SUPERCONDUCTING PAIRING CHANNELS

For the A_{1u} and A_{2u} channels, the symmetry data vector is given by $\boldsymbol{B}^{\mathrm{BdG}} = \boldsymbol{B} - \boldsymbol{B}^{\mathrm{vac}}$, with $\boldsymbol{B}^{\mathrm{vac}} = (0,0,2,2,0,0,2,2,0,4)$. The refined EBR matrix is given by $\{\mathcal{EBR}\}^{\mathrm{BdG}} = \mathcal{EBR} - \overline{\mathcal{EBR}}$, with

$$\overline{\mathcal{EBR}} = \begin{pmatrix} 0&0&1&0&0&0&1&0&0&1 \\ 0&0&0&1&0&0&0&1&0&1 \\ 1&0&0&0&1&0&0&0&1&0 \\ 0&1&0&0&0&1&0&0&1&0 \\ 0&0&1&0&0&0&0&1&1&0 \\ 0&0&0&1&0&0&1&0&1&0 \\ 1&0&0&0&0&1&0&0&0&1 \\ 0&1&0&0&1&0&0&0&0&1 \\ 0&0&1&1&1&1&0&0&1&1 \\ 1&1&0&0&0&0&1&1&1&1 \end{pmatrix} \tag{46}$$

Such that the refined EBR matrix also admits the Smith normal decomposition:

$$\left(L^{\mathrm{BdG}}_{\mathcal{EBR}}\right)^{-1} = \begin{pmatrix} 1&1&0&0&0&-1&0&0&0&0 \\ 0&1&0&0&0&0&0&0&0&0 \\ 0&1&0&0&1&0&0&0&-1&0 \\ 0&2&0&0&1&-1&0&0&-1&0 \\ 1&-3&0&0&-3&1&0&0&2&0 \\ 1&0&1&0&0&0&0&0&0&0 \\ 0&0&0&0&1&0&1&0&0&0 \\ 0&0&0&0&0&1&0&1&0&0 \\ 0&1&0&1&0&0&0&0&0&0 \\ 0&0&0&0&0&0&0&0&1&1 \end{pmatrix}, \tag{47}$$

$$\Lambda^{\mathrm{BdG}}_{\mathcal{EBR}} = \begin{pmatrix} 1&0&0&0&0&0&0&0&0&0 \\ 0&1&0&0&0&0&0&0&0&0 \\ 0&0&1&0&0&0&0&0&0&0 \\ 0&0&0&2&0&0&0&0&0&0 \\ 0&0&0&0&8&0&0&0&0&0 \\ 0&0&0&0&0&0&0&0&0&0 \\ 0&0&0&0&0&0&0&0&0&0 \\ 0&0&0&0&0&0&0&0&0&0 \\ 0&0&0&0&0&0&0&0&0&0 \\ 0&0&0&0&0&0&0&0&0&0 \end{pmatrix}, \tag{48}$$

$$\left(R^{\mathrm{BdG}}_{\mathcal{EBR}}\right)^{-1} = \begin{pmatrix} 1&0&0&-3&-5&0&0&0&1&0 \\ 0&1&0&-1&-1&1&0&0&0&0 \\ 0&0&0&0&0&0&0&0&1&0 \\ 0&0&0&0&0&1&0&0&0&0 \\ 0&0&1&0&3&0&1&0&0&0 \\ 0&0&0&0&-1&0&0&1&0&0 \\ 0&0&0&0&0&0&1&0&0&0 \\ 0&0&0&0&0&0&0&1&0&0 \\ 0&0&0&1&2&0&0&0&0&1 \\ 0&0&0&0&0&0&0&0&0&1 \end{pmatrix}. \tag{49}$$

The double SI group of the superconducting states respecting Type-II SLG $p4/mmm1'$ in the A_{1u} and A_{2u} pairing channels is $X^{\mathrm{BdG}}_{\mathrm{BS}} = \mathbb{Z}_2 \times \mathbb{Z}_8$ and given by

$$z_2 = 2m(\bar{\Gamma}_7) + m(\bar{M}_6) - m(\bar{M}_7) - m(\bar{X}_5) \mod 2, \tag{50}$$

$$z_8 = m(\bar{\Gamma}_6) - 3m(\bar{\Gamma}_7) - 3m(\bar{M}_6) + m(\bar{M}_7) + 2m(\bar{X}_5) \mod 8. \tag{51}$$

7. REFINED SI GROUP IN THE B_{1u} AND B_{2u} SUPERCONDUCTING PAIRING CHANNELS

For the B_{1u} and B_{2u} channels, the symmetry data vector is given by $\boldsymbol{B}^{\mathrm{BdG}} = \boldsymbol{B} - \boldsymbol{B}^{\mathrm{vac}}$, with $\boldsymbol{B}^{\mathrm{vac}} = (0,0,2,2,0,0,2,2,0,4)$. The refined EBR matrix is given by $\{\mathcal{EBR}\}^{\mathrm{BdG}} = \mathcal{EBR} - \overline{\mathcal{EBR}}$ with

$$\overline{\mathcal{EBR}} = \begin{pmatrix} 0&0&0&1&0&0&0&1&0&1 \\ 0&0&1&0&0&0&1&0&0&1 \\ 0&1&0&0&0&1&0&0&1&0 \\ 1&0&0&0&1&0&0&0&1&0 \\ 0&0&0&1&0&0&1&0&1&0 \\ 0&0&1&0&0&0&0&1&1&0 \\ 0&1&0&0&1&0&0&0&0&1 \\ 1&0&0&0&0&1&0&0&0&1 \\ 0&0&1&1&1&1&0&0&1&1 \\ 1&1&0&0&0&0&1&1&1&1 \end{pmatrix}. \tag{52}$$

Such that the refined EBR matrix also admits the Smith normal decomposition:

$$\left(L^{\mathrm{BdG}}_{\mathcal{EBR}}\right)^{-1} = \begin{pmatrix} 1&1&0&0&0&-1&0&0&0&0 \\ 0&1&0&0&0&0&0&0&0&0 \\ 0&1&0&0&1&0&0&0&-1&0 \\ 0&2&0&0&1&-1&0&0&-1&0 \\ 1&-3&0&0&-3&1&0&0&2&0 \\ 0&1&1&0&0&0&0&0&0&0 \\ 0&0&0&0&0&1&1&0&0&0 \\ 0&0&0&0&1&0&0&1&0&0 \\ 1&0&0&1&0&0&0&0&0&0 \\ 0&0&0&0&0&0&0&0&1&1 \end{pmatrix}, \tag{53}$$

$$\Lambda^{\mathrm{BdG}}_{\mathcal{EBR}} = \begin{pmatrix} 1&0&0&0&0&0&0&0&0&0 \\ 0&1&0&0&0&0&0&0&0&0 \\ 0&0&1&0&0&0&0&0&0&0 \\ 0&0&0&2&0&0&0&0&0&0 \\ 0&0&0&0&8&0&0&0&0&0 \\ 0&0&0&0&0&0&0&0&0&0 \\ 0&0&0&0&0&0&0&0&0&0 \\ 0&0&0&0&0&0&0&0&0&0 \\ 0&0&0&0&0&0&0&0&0&0 \\ 0&0&0&0&0&0&0&0&0&0 \end{pmatrix}, \tag{54}$$

$$\left(R^{\mathrm{BdG}}_{\mathcal{EBR}}\right)^{-1} = \begin{pmatrix} 1&0&0&-3&-5&1&0&0&0&0 \\ 0&1&0&-1&-1&0&0&0&1&0 \\ 0&0&0&0&0&0&0&0&1&0 \\ 0&0&0&0&0&1&0&0&0&0 \\ 0&0&1&0&3&0&0&1&0&0 \\ 0&0&0&0&-1&0&1&0&0&0 \\ 0&0&0&0&0&0&1&0&0&0 \\ 0&0&0&0&0&0&0&1&0&0 \\ 0&0&0&1&2&0&0&0&0&1 \\ 0&0&0&0&0&0&0&0&0&1 \end{pmatrix}. \tag{55}$$

The double SI group of the superconducting states respecting Type-II SLG $p4/mmm1'$ in the B_{1u} and B_{2u} pairing channels is $X^{\mathrm{BdG}}_{\mathrm{BS}} = \mathbb{Z}_2 \times \mathbb{Z}_8$ and given by

$$z_2 = 2m(\bar{\Gamma}_7) + m(\bar{M}_6) - m(\bar{M}_7) - m(\bar{X}_5) \mod 2, \tag{56}$$

$$z_8 = m(\bar{\Gamma}_6) - 3m(\bar{\Gamma}_7) - 3m(\bar{M}_6) + m(\bar{M}_7) + 2m(\bar{X}_5) \mod 8. \tag{57}$$

8. BAND STRUCTURE OF THE NORMAL STATE

In this section, we illustrate the band coreps of the normal state to systematically study the topological superconducting property of the eight one-dimensional pairing channel in $La_3Ni_2O_7$, as shown in Fig. 1.

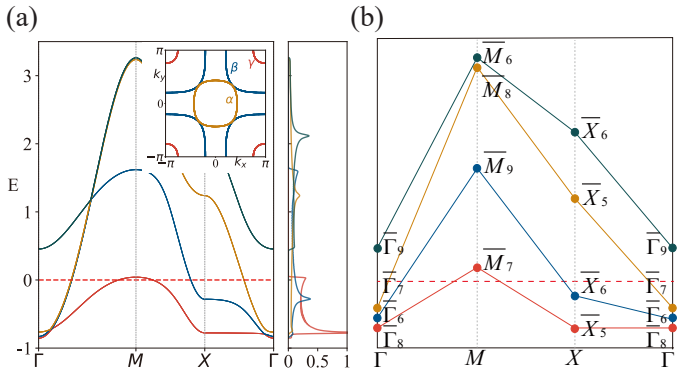

FIG. 1. (a) Band structure of the bilayer two-orbital model. The subfigures show the Fermi surface and the normalized DOS of each band. (b) Corresponding band coreps.

9. PAIRINGS IN THE A_{1g} CHANNEL

In this section, we present the symmetry-allowed mean-field superconducting pairings in the A_{1g} pairing channel, as listed in Tab. II. In Fig. 2(a), we show the saddle-point solutions of the self-consistent gap equation for these mean-field superconducting pairings. In Fig. 2(b), we present the free energy of the favored pairings, with attractive potential strength $V = 0.5$ eV. In Figs. 2(c)-(d), we illustrate the band structure and the corresponding band coreps.

TABLE II. List of symmetry-allowed mean-field superconducting pairings in the A_{1g} pairing channel.

$\mathcal{H}_\Delta$ in the A_{1g} pairing channel	
$\Delta_0\tau_y\rho_0(\frac{\sigma_0+\sigma_z}{2})s_y$	$\Delta_8\left[(\cos k_x+\cos k_y)\,\tau_y\rho_0(\sigma_0+\sigma_z)s_y\right]$
$\Delta_1\tau_y\rho_x(\frac{\sigma_0+\sigma_z}{2})s_y$	$2\Delta_9\left[(\cos k_x-\cos k_y)\,\tau_y\rho_0\sigma_x s_y\right]$
$\Delta_2\tau_y\rho_0(\frac{\sigma_0-\sigma_z}{2})s_y$	$\Delta_{10}\left[(\cos k_x+\cos k_y)\,\tau_y\rho_x(\sigma_0+\sigma_z)s_y\right]$
$\Delta_3\tau_y\rho_x(\frac{\sigma_0-\sigma_z}{2})s_y$	$2\Delta_{11}\left[(\cos k_x-\cos k_y)\,\tau_y\rho_x\sigma_x s_y\right]$
$\Delta_4\left[\sin k_x\tau_y\rho_z(\sigma_0+\sigma_z)s_0-\sin k_y\tau_x\rho_z(\sigma_0+\sigma_z)s_z\right]$	$\Delta_{12}\left[(\cos k_x+\cos k_y)\,\tau_y\rho_0(\sigma_0-\sigma_z)s_y\right]$
$2\Delta_5\left(\sin k_x\tau_y\rho_z\sigma_x s_0+\sin k_y\tau_x\rho_z\sigma_x s_z\right)$	$\Delta_{13}\left[(\cos k_x+\cos k_y)\,\tau_y\rho_x\,(\sigma_0-\sigma_z)\,s_y\right]$
$2\Delta_6\left(\sin k_x\tau_y\rho_y\sigma_y s_0+\sin k_y\tau_x\rho_y\sigma_y s_z\right)$	$4\Delta_{14}\sin k_x\sin k_y\tau_x\rho_0\sigma_y s_x$
$\Delta_7\left[\sin k_x\tau_y\rho_z(\sigma_0-\sigma_z)s_0-\sin k_y\tau_x\rho_z(\sigma_0-\sigma_z)s_z\right]$	

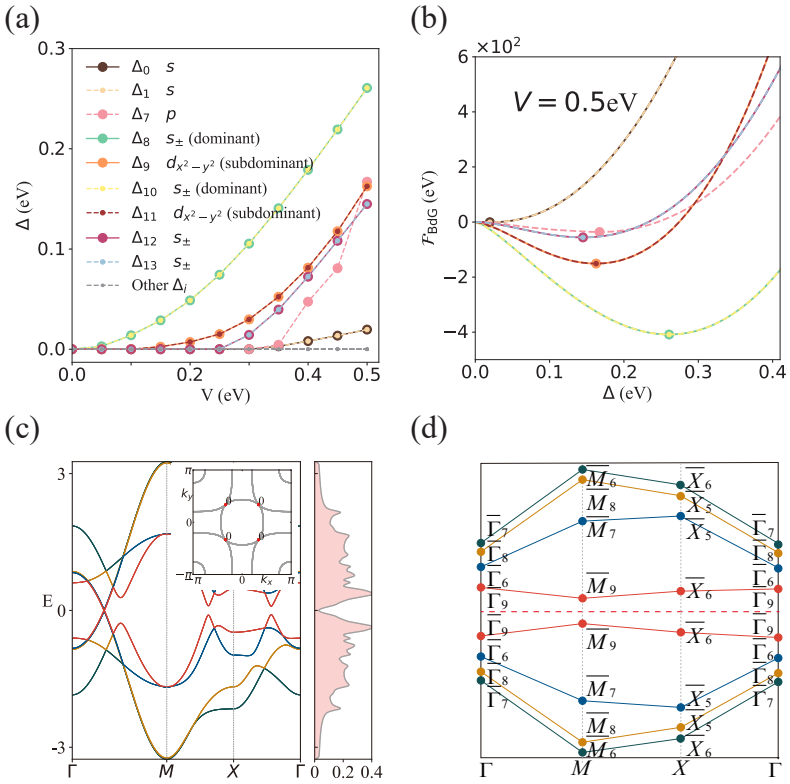

FIG. 2. (a) Pairing strength Δ_i vs V_i obtained by solving the self-consistent equations for the A_{1g} pairing channel . The result shows that Δ_8 and Δ_{10} pairings are the primarily favored, while the Δ_9 and Δ_{11} pairings are secondly favored. (b) BdG condensation energy $\mathcal{F}_{\rm BdG}$ vs $|\Delta_i|$ at $V_i = 0.5$ eV. (c) Bulk spectrum of the superconducting state of $La_3Ni_2O_7$. (d) Band coreps of the bulk spectrum. The parameters are $\Delta_8 = 0.2607473$ eV, $\Delta_{10} = 0.1607473$ eV, $\Delta_9 = 0.1625672$ eV, and $\Delta_{11} = 0.0625672$ eV.

10. PAIRINGS IN THE A_{2g} CHANNEL

In this section, we present the symmetry-allowed mean-field superconducting pairings in the A_{2g} pairing channel, as listed in Tab. III. In Fig. 3(a), we show the saddle-point solutions of the self-consistent gap equation for these mean-field superconducting pairings. In Fig. 3(b), we present the free energy of the favored pairings, with attractive potential strength $V = 0.5$ eV. In Figs. 3(c)-(d), we illustrate the band structure and the corresponding band coreps.

TABLE III. List of symmetry-allowed mean-field superconducting pairings in the A_{2g} pairing channel.

$\mathcal{H}_\Delta$ in the A_{2g} pairing channel
$\Delta_0 \left[\sin k_x \tau_x \rho_z (\sigma_0 + \sigma_z) s_z + \sin k_y \tau_y \rho_z (\sigma_0 + \sigma_z) s_0\right]$
$2\Delta_1 \left(\sin k_x \tau_x \rho_z \sigma_x s_z - \sin k_y \tau_y \rho_z \sigma_x s_0\right)$
$2\Delta_2 \left(\sin k_x \tau_x \rho_y \sigma_y s_z - \sin k_y \tau_y \rho_y \sigma_y s_0\right)$
$\Delta_3 \left[\sin k_x \tau_x \rho_z (\sigma_0 - \sigma_z) s_z + \sin k_y \tau_y \rho_z (\sigma_0 - \sigma_z) s_0\right]$
$2\Delta_4 \left(\cos k_x - \cos k_y\right) \tau_x \rho_0 \sigma_y s_x$
$2\Delta_5 \left(\cos k_x - \cos k_y\right) \tau_x \rho_x \sigma_y s_x$
$4\Delta_6 \sin k_x \sin k_y \tau_y \rho_0 \sigma_x s_y$
$4\Delta_7 \sin k_x \sin k_y \tau_y \rho_x \sigma_x s_y$

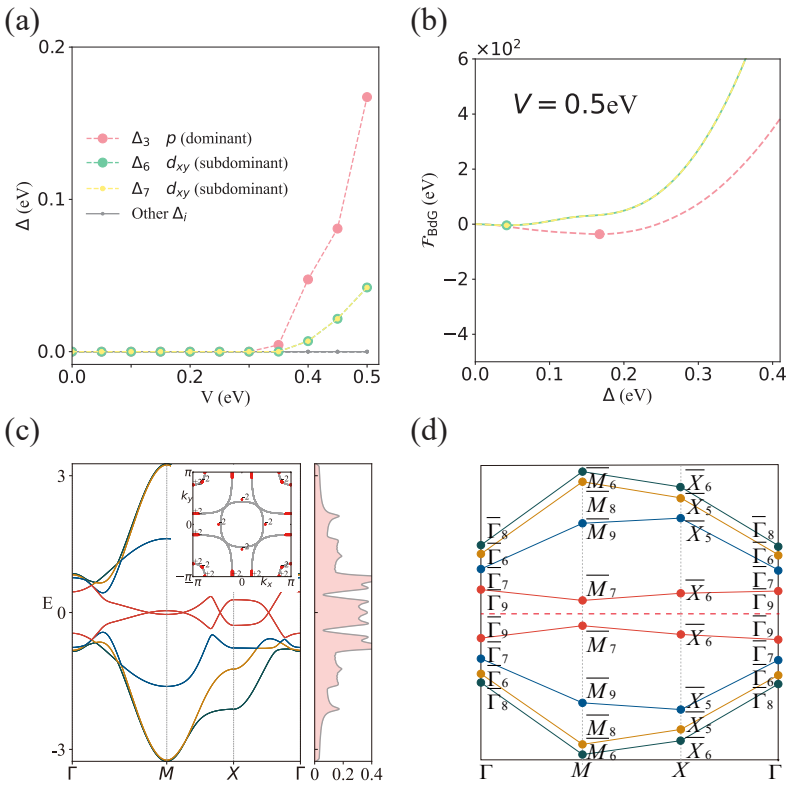

FIG. 3. (a) Pairing strength Δ_i vs V_i obtained by solving the self-consistent equations for the A_{2g} pairing channel. The result shows that Δ_3 pairing is the primarily favored, while the Δ_6 and Δ_{10} pairings are secondly favored. (b) BdG condensation energy $\mathcal{F}_{\rm BdG}$ vs $|\Delta_i|$ at $V_i = 0.5$ eV. (c) Bulk spectrum of the superconducting state of $La_3Ni_2O_7$. (d) Band coreps of the bulk spectrum. The parameters are $\Delta_3 = 0.1671629$ eV, $\Delta_6 = 0.04214721$ eV, and $\Delta_7 = 0.04214721$ eV.

11. PAIRINGS IN THE B_{1g} CHANNEL

In this section, we present the symmetry-allowed mean-field superconducting pairings in the B_{1g} pairing channel, as listed in Tab. IV. In Fig. 4(a), we show the saddle-point solutions of the self-consistent gap equation for these mean-field superconducting pairings. In Fig. 4(b), we present the BdG condensation energy of the favored pairings, with attractive potential strength $V = 0.5$ eV. In Figs. 4(c)-(d), we illustrate the band structure and the corresponding band coreps.

TABLE IV. List of symmetry-allowed mean-field superconducting pairings in the B_{1g} pairing channel.

$\mathcal{H}_\Delta$ in the B_{1g} pairing channel	
$\Delta_0\tau_y\rho_0\sigma_x s_y$	$\Delta_8\left[(\cos k_x-\cos k_y)\,\tau_y\rho_x(\sigma_0+\sigma_z)s_y\right]$
$\Delta_1\tau_y\rho_x\sigma_x s_y$	$2\Delta_9\left[(\cos k_x+\cos k_y)\,\tau_y\rho_x\sigma_x s_y\right]$
$\Delta_2\left[\sin k_x\tau_y\rho_z(\sigma_0+\sigma_z)s_0+\sin k_y\tau_x\rho_z(\sigma_0+\sigma_z)s_z\right]$	$\Delta_{10}\left[(\cos k_x-\cos k_y)\,\tau_y\rho_0(\sigma_0-\sigma_z)s_y\right]$
$2\Delta_3\left(\sin k_x\tau_y\rho_z\sigma_x s_0-\sin k_y\tau_x\rho_z\sigma_x s_z\right)$	$\Delta_{11}\left[(\cos k_x-\cos k_y)\,\tau_y\rho_x(\sigma_0-\sigma_z)s_y\right]$
$2\Delta_4\left(\sin k_x\tau_y\rho_y\sigma_y\tau_0-\sin k_y\tau_x\rho_y\sigma_y\tau_z\right)$	
$\Delta_5\left[\sin k_x\tau_y\rho_z(\sigma_0-\sigma_z)s_0+\sin k_y\tau_x\rho_z(\sigma_0-\sigma_z)s_z\right]$	
$\Delta_6\left[(\cos k_x-\cos k_y)\,\tau_y\rho_0(\sigma_0+\sigma_z)s_y\right]$	
$2\Delta_7\left[(\cos k_x+\cos k_y)\,\tau_y\rho_0\sigma_x s_y\right]$	

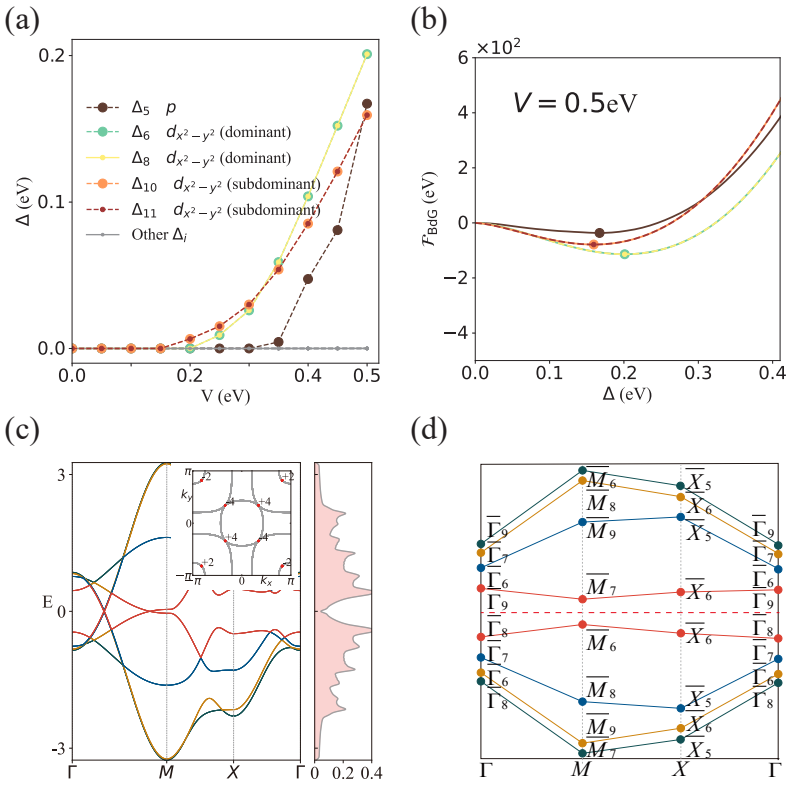

FIG. 4. (a) Pairing strength Δ_i vs V_i obtained by solving the self-consistent equations for the B_{1g} pairing channel. The result shows that Δ_6 and Δ_8 pairing is the primarily favored, while the Δ_{10} and Δ_{11} pairings are secondly favored. (b) BdG condensation energy $\mathcal{F}_{\rm BdG}$ vs $|\Delta_i|$ at $V_i = 0.5$ eV. (c) Bulk spectrum of the superconducting state of $La_3Ni_2O_7$. (d) Band coreps of the bulk spectrum. The parameters are $\Delta_6 = 0.3009957$ eV, $\Delta_8 = 0.2009957$eV, $\Delta_{10} = 0.1593723$eV, and $\Delta_{11} = 0.0593723$eV.

12. PAIRINGS IN THE B_{2g} CHANNEL

In this section, we present the symmetry-allowed mean-field superconducting pairings in the B_{2g} pairing channel, as listed in Tab. V. In Fig. 5(a), we show the saddle-point solutions of the self-consistent gap equation for these mean-field superconducting pairings. In Fig. 5(b), we present the BdG condensation energy of the favored pairings, with attractive potential strength $V = 0.5$ eV. In Figs. 5(c)-(d), we illustrate the band structure and the corresponding band coreps.

TABLE V. List of symmetry-allowed mean-field superconducting pairings in the B_{2g} pairing channel.

$\mathcal{H}_\Delta$ in the B_{2g} pairing channel	
$\Delta_0\tau_y\rho_0\sigma_y s_x$	$2\Delta_8 \sin k_x \sin k_y \tau_y\rho_0(\sigma_0+\sigma_z)s_y$
$\Delta_1\tau_x\rho_x\sigma_y s_x$	$2\Delta_9 \sin k_x \sin k_y \tau_y\rho_x(\sigma_0+\sigma_z)s_y$
$\Delta_2 [\sin k_x\tau_x\rho_z(\sigma_0+\sigma_z)s_z - \sin k_y\tau_y\rho_z(\sigma_0+\sigma_z)s_0]$	$2\Delta_{10} \sin k_x \sin k_y \tau_y\rho_0(\sigma_0-\sigma_z)s_y$
$2\Delta_3 (\sin k_x\tau_x\rho_z\sigma_x\tau_z + \sin k_y\tau_y\rho_z\sigma_x\tau_0)$	$2\Delta_{11} \sin k_x \sin k_y \tau_y\rho_x(\sigma_0-\sigma_z)s_y$
$2\Delta_4 (\sin k_x\tau_x\rho_y\sigma_y\tau_z - \sin k_y\tau_y\rho_y\sigma_y\tau_0)$	
$\Delta_5 [\sin k_x\tau_x\rho_z(\sigma_0-\sigma_z)s_z - \sin k_y\tau_y\rho_z(\sigma_0-\sigma_z)s_0]$	
$2\Delta_6 [(\cos k_x + \cos k_y)\tau_x\rho_0\sigma_y s_x]$	
$2\Delta_7 [(\cos k_x + \cos k_y)\tau_x\rho_x\sigma_y s_x]$	

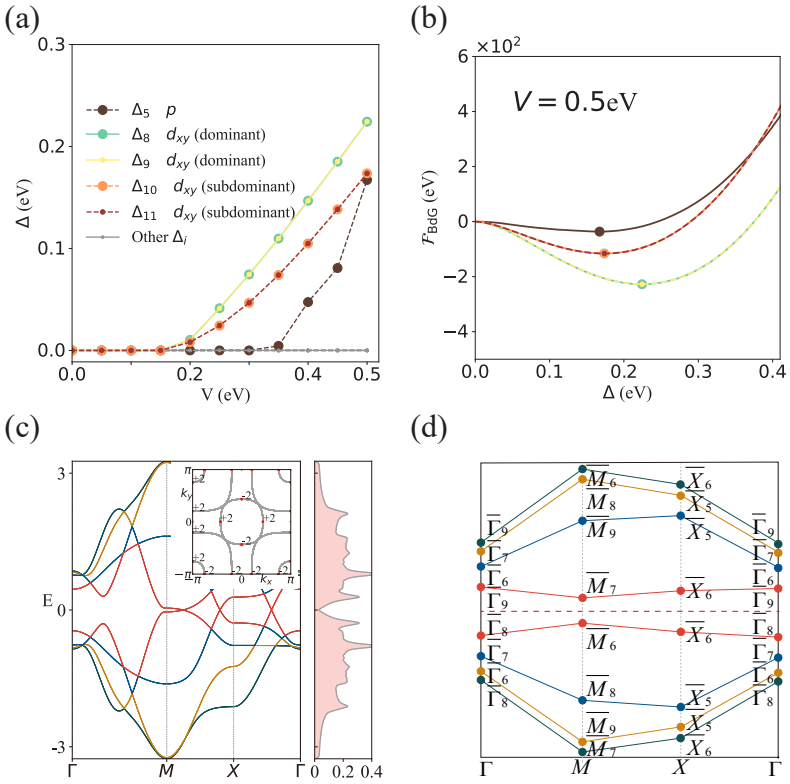

FIG. 5. (a) Pairing strength Δ_i vs V_i obtained by solving the self-consistent equations for the B_{2g} pairing channel. The result shows that Δ_8 and Δ_9 pairing is the primarily favored, while the Δ_{10} and Δ_{11} pairings are secondly favored. (b) BdG condensation energy $\mathcal{F}_{\rm BdG}$ vs $|\Delta_i|$ at $V_i = 0.5$ eV. (c) Bulk spectrum of the superconducting state of $La_3Ni_2O_7$. (d) Band coreps of the bulk spectrum. The parameters are $\Delta_8 = 0.3243310$ eV, $\Delta_8 = 0.2243310$eV, $\Delta_{10} = 0.2736426$eV, and $\Delta_{11} = 0.1736426$eV.

13. PAIRINGS IN THE A_{1u} CHANNEL

In this section, we present the symmetry-allowed mean-field superconducting pairings in the A_{1u} pairing channel, as listed in Tab. VI. In Fig. 6(a), we show the saddle-point solutions of the self-consistent gap equation for these mean-field superconducting pairings. In Fig. 6(b), we present the free energy of the favored pairings, with attractive potential strength $V = 0.5$ eV. In Figs. 6(c)-(d), we illustrate the band structure and the corresponding band coreps.

TABLE VI. List of symmetry-allowed mean-field superconducting pairings in the A_{1u} pairing channel.

$\mathcal{H}_\Delta$ in the A_{1u} pairing channel	
$\Delta_0\tau_x\rho_y(\frac{\sigma_0+\sigma_z}{2})s_x$	$4\Delta_8 \sin k_x \sin k_y\tau_y\rho_z\sigma_x s_y$
$\Delta_1\tau_x\rho_y(\frac{\sigma_0-\sigma_z}{2})s_x$	$4\Delta_9 \sin k_x \sin k_y\tau_y\rho_y\sigma_y s_y$
$\Delta_2 [\sin k_x\tau_x\rho_0(\sigma_0+\sigma_z)s_z + \sin k_y\tau_y\rho_0(\sigma_0+\sigma_z)s_0]$	$2\Delta_{10} [(\cos k_x - \cos k_y)\tau_x\rho_z\sigma_y s_x]$
$2\Delta_3 (\sin k_x\tau_x\rho_0\sigma_x s_z - \sin k_y\tau_y\rho_0\sigma_x s_0)$	$\Delta_{11} [(\cos k_x + \cos k_y)\tau_x\rho_y(\sigma_0+\sigma_z)s_x]$
$\Delta_4 [\sin k_x\tau_x\rho_x(\sigma_0+\sigma_z)s_z + \sin k_y\tau_y\rho_x(\sigma_0+\sigma_z)s_0]$	$2\Delta_{12} [(\cos k_x - \cos k_y)\tau_x\rho_y\sigma_x s_x]$
$2\Delta_5 (\sin k_x\tau_x\rho_x\sigma_x s_z - \sin k_y\tau_y\rho_x\sigma_x s_0)$	$\Delta_{13} [(\cos k_x + \cos k_y)\tau_x\rho_y(\sigma_0-\sigma_z)s_x]$
$\Delta_6 [\sin k_x\tau_x\rho_0(\sigma_0-\sigma_z)s_z + \sin k_y\tau_y\rho_0(\sigma_0-\sigma_z)s_0]$	
$\Delta_7 [\sin k_x\tau_x\rho_x(\sigma_0-\sigma_z)s_z + \sin k_y\tau_y\rho_x(\sigma_0-\sigma_z)s_0]$	

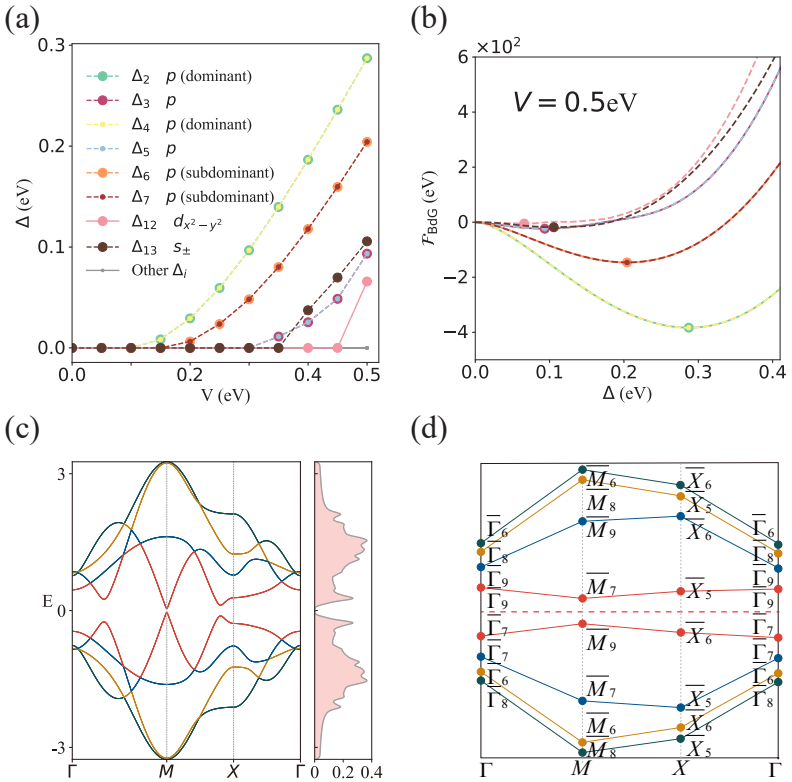

FIG. 6. (a) Pairing strength Δ_i vs V_i obtained by solving the self-consistent equations for the A_{1u} pairing channel. The result shows that Δ_2 and Δ_4 pairing is the primarily favored, while the Δ_6 and Δ_7 pairings are secondly favored. (b) BdG condensation energy $\mathcal{F}_{\rm BdG}$ vs $|\Delta_i|$ at $V_i = 0.5$ eV. (c) Bulk spectrum of the superconducting state of $La_3Ni_2O_7$. (d) Band coreps of the bulk spectrum. The parameters are $\Delta_2 = 0.3871102$, $\Delta_4 = 0.2871102$eV, $\Delta_6 = 0.3041629$eV, and $\Delta_7 = 0.2041629$eV.

14. PAIRINGS IN THE A_{2u} CHANNEL

In this section, we present the symmetry-allowed mean-field superconducting pairings in the A_{2u} pairing channel, as listed in Tab. VII. In Fig. 7(a), we show the saddle-point solutions of the self-consistent gap equation for these mean-field superconducting pairings. In Fig. 7(b), we present the BdG condensation energy of the favored pairings, with attractive potential strength $V = 0.5$ eV. In Figs. 7(c)-(d), we illustrate the band structure and the corresponding band coreps.

TABLE VII. List of symmetry-allowed mean-field superconducting pairings in the A_{2u} pairing channel.

$\mathcal{H}_\Delta$ in the A_{2u} pairing channel	
$\Delta_0\tau_y\rho_z(\frac{\sigma_0+\sigma_z}{2})s_y$	$\Delta_8\left[(\cos k_x+\cos k_y)\,\tau_y\rho_z(\sigma_0+\sigma_z)s_y\right]$
$\Delta_1\tau_y\rho_z(\frac{\sigma_0-\sigma_z}{2})s_y$	$2\Delta_9\left[(\cos k_x-\cos k_y)\,\tau_y\rho_z\sigma_x s_y\right]$
$\Delta_2\left[\sin k_x\tau_y\rho_0(\sigma_0+\sigma_z)s_0-\sin k_y\tau_x\rho_0(\sigma_0+\sigma_z)s_z\right]$	$2\Delta_{10}\left[(\cos k_x-\cos k_y)\,\tau_y\rho_y\sigma_y s_y\right]$
$2\Delta_3\left(\sin k_x\tau_y\rho_0\sigma_x s_0+\sin k_y\tau_x\rho_0\sigma_x s_z\right)$	$\Delta_{11}\left[(\cos k_x+\cos k_y)\,\tau_y\rho_z(\sigma_0-\sigma_z)s_y\right]$
$\Delta_4\left[\sin k_x\tau_y\rho_x(\sigma_0+\sigma_z)s_0-\sin k_y\tau_x\rho_x(\sigma_0+\sigma_z)s_z\right]$	$4\Delta_{12}\sin k_x\sin k_y\tau_x\rho_z\sigma_y s_x$
$2\Delta_5\left(\sin k_x\tau_y\rho_x\sigma_x s_0+\sin k_y\tau_x\rho_x\sigma_x s_z\right)$	$4\Delta_{13}\sin k_x\sin k_y\tau_x\rho_y\sigma_x s_x$
$\Delta_6\left[\sin k_x\tau_y\rho_0(\sigma_0-\sigma_z)s_0-\sin k_y\tau_x\rho_0(\sigma_0-\sigma_z)s_z\right]$	
$\Delta_7\left[\sin k_x\tau_y\rho_x(\sigma_0-\sigma_z)s_0-\sin k_y\tau_x\rho_x(\sigma_0-\sigma_z)s_z\right]$	

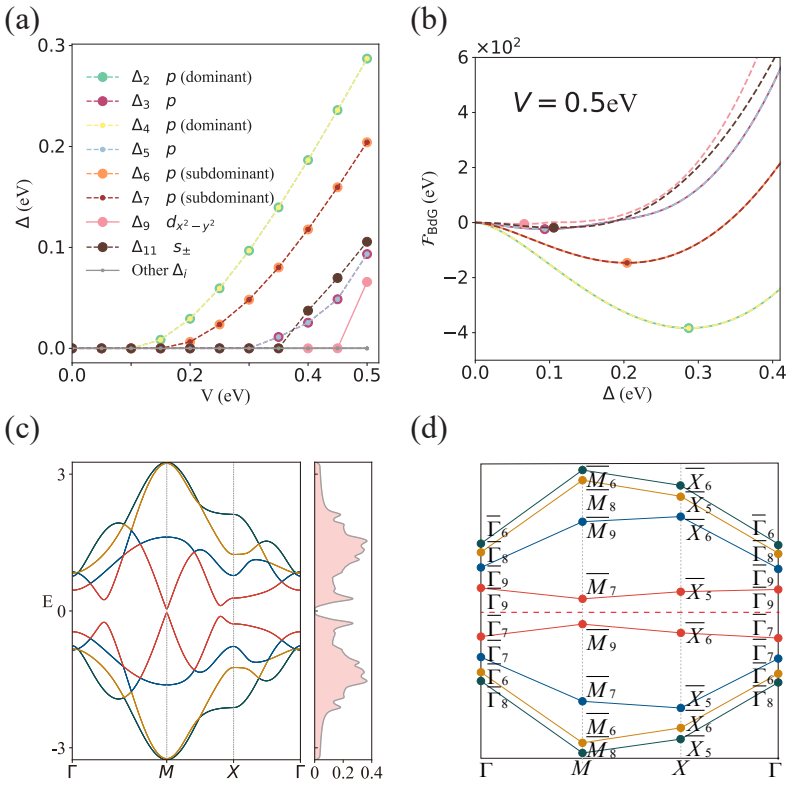

FIG. 7. (a) Pairing strength Δ_i vs V_i obtained by solving the self-consistent equations for the A_{2u} pairing channel. The result shows that Δ_2 and Δ_4 pairing is the primarily favored, while the Δ_6 and Δ_7 pairings are secondly favored. (b)BdG condensation energy $\mathcal{F}_{\rm BdG}$ vs $|\Delta_i|$ at $V_i = 0.5$ eV. (c) Bulk spectrum of the superconducting state of $La_3Ni_2O_7$. (d) Band coreps of the bulk spectrum. The parameters are $\Delta_2 = 0.3871102$, $\Delta_4 = 0.2871102$eV, $\Delta_6 = 0.3041629$eV, and $\Delta_7 = 0.2041629$eV.

15. PAIRINGS IN THE B_{1u} CHANNEL

In this section, we present the symmetry-allowed mean-field superconducting pairings in the B_{1u} pairing channel, as listed in Tab. VIII. In Fig. 8(a), we show the saddle-point solutions of the self-consistent gap equation for these mean-field superconducting pairings. In Fig. 8(b), we present the BdG condensation energy of the favored pairings, with attractive potential strength $V = 0.5$ eV. In Figs. 8(c)-(d), we illustrate the band structure and the corresponding band coreps.

TABLE VIII. List of symmetry-allowed mean-field superconducting pairings in the B_{1u} pairing channel.

$\mathcal{H}_\Delta$ in the B_{1u} pairing channel	
$\Delta_0\tau_x\rho_z\sigma_y s_x$	$\Delta_8\left[(\cos k_x-\cos k_y)\,\tau_x\rho_y(\sigma_0+\sigma_z)s_x\right]$
$\Delta_1\tau_x\rho_y\sigma_x s_x$	$2\Delta_9\left[(\cos k_x+\cos k_y)\,\tau_x\rho_z\sigma_y s_x\right]$
$\Delta_2\left[\sin k_x\tau_x\rho_0(\sigma_0+\sigma_z)s_z-\sin k_y\tau_y\rho_0(\sigma_0+\sigma_z)s_0\right]$	$2\Delta_{10}\left[(\cos k_x+\cos k_y)\,\tau_x\rho_y\sigma_x s_x\right]$
$2\Delta_3\left[\sin k_x\tau_x\rho_0\sigma_x s_z+\sin k_y\tau_y\rho_0\sigma_x s_0\right]$	$\Delta_{11}\left[(\cos k_x-\cos k_y)\,\tau_x\rho_y(\sigma_0-\sigma_z)s_x\right]$
$\Delta_4\left[\sin k_x\tau_x\rho_x(\sigma_0+\sigma_z)s_z-\sin k_y\tau_y\rho_x(\sigma_0+\sigma_z)s_0\right]$	$\Delta_{12}\left[2\sin k_x\sin k_y\tau_y\rho_z\,(\sigma_0+\sigma_z)\,s_y\right]$
$2\Delta_5\left[\sin k_x\tau_x\rho_x\sigma_x s_z+\sin k_y\tau_y\rho_x\sigma_x s_0\right]$	$\Delta_{13}\left[2\sin k_x\sin k_y\tau_y\rho_z\,(\sigma_0-\sigma_z)\,s_y\right]$
$\Delta_6\left[\sin k_x\tau_x\rho_0(\sigma_0-\sigma_z)s_z-\sin k_y\tau_y\rho_0(\sigma_0-\sigma_z)s_0\right]$	
$\Delta_7\left[\sin k_x\tau_x\rho_x(\sigma_0-\sigma_z)s_z-\sin k_y\tau_y\rho_x(\sigma_0-\sigma_z)s_0\right]$	

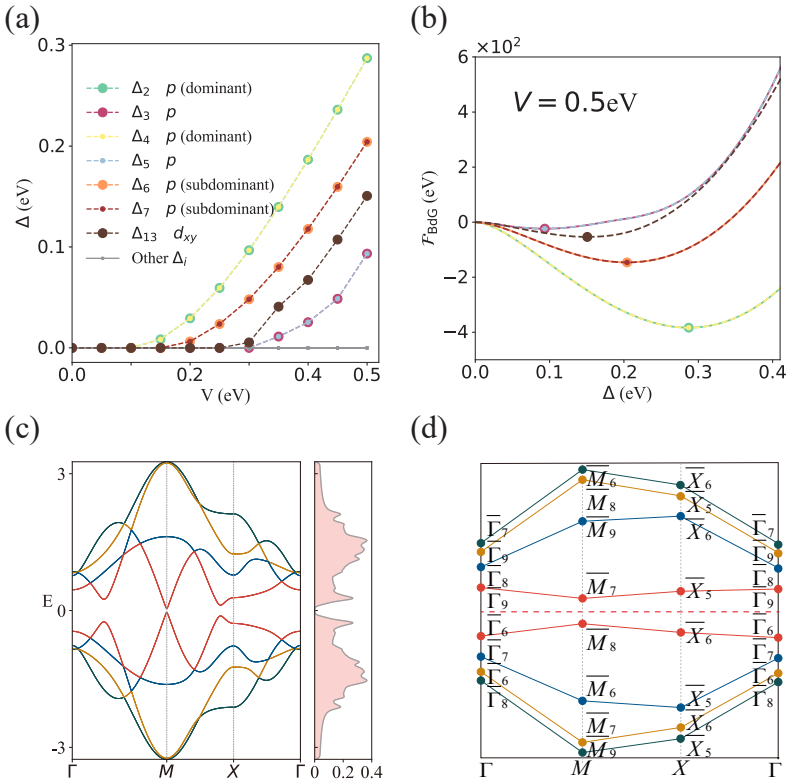

FIG. 8. (a) Pairing strength Δ_i vs V_i obtained by solving the self-consistent equations for the B_{1u} pairing channel . The result shows that Δ_2 and Δ_4 pairings are primarily favored, while the Δ_6 and Δ_7 pairings are secondly favored. (b) BdG condensation energy $\mathcal{F}_{\rm BdG}$ vs $|\Delta_i|$ at $V_i = 0.5$ eV. (c) Bulk spectrum of the superconducting state of $La_3Ni_2O_7$. (d) Band coreps of the bulk spectrum. The parameters are $\Delta_2 = 0.3871102$, $\Delta_4 = 0.2871102$eV, $\Delta_6 = 0.3041629$eV, and $\Delta_7 = 0.2041629$eV.

16. PAIRINGS IN THE B_{2u} CHANNEL

In this section, we present the symmetry-allowed mean-field superconducting pairings in the B_{2u} pairing channel, as listed in Tab. IX. In Fig. 9(a), we show the saddle-point solutions of the self-consistent gap equation for these mean-field superconducting pairings. In Fig. 9(b), we present the BdG condensation energy of the favored pairings, with attractive potential strength $V = 0.5$ eV. In Figs. 9(c)-(d), we illustrate the band structure and the corresponding band coreps.

TABLE IX. List of symmetry-allowed mean-field superconducting pairings in B_{2u} pairing channel.

$\mathcal{H}_\Delta$ in B_{2u} pairing channel	
$\Delta_0\tau_y\rho_z\sigma_x s_y$	$\Delta_8\left[(\cos k_x-\cos k_y)\,\tau_y\rho_z(\sigma_0+\sigma_z)s_y\right]$
$\Delta_1\tau_y\rho_y\sigma_y s_y$	$2\Delta_9\left[(\cos k_x+\cos k_y)\,\tau_y\rho_z\sigma_x s_y\right]$
$\Delta_2\left[\sin k_x\tau_y\rho_0(\sigma_0+\sigma_z)s_0+\sin k_y\tau_x\rho_0(\sigma_0+\sigma_z)s_z\right]$	$2\Delta_{10}\left[(\cos k_x+\cos k_y)\,\tau_y\rho_y\sigma_y s_y\right]$
$2\Delta_3\left[\sin k_x\tau_y\rho_0\sigma_x s_0-\sin k_y\tau_x\rho_0\sigma_x s_z\right]$	$\Delta_{11}\left[(\cos k_x-\cos k_y)\,\tau_y\rho_z(\sigma_0-\sigma_z)s_y\right]$
$\Delta_4\left[\sin k_x\tau_y\rho_x(\sigma_0+\sigma_z)s_0+\sin k_y\tau_x\rho_x(\sigma_0+\sigma_z)s_z\right]$	$\Delta_{12}\left[2\sin k_x\sin k_y\tau_x\rho_y\,(\sigma_0+\sigma_z)\,s_x\right]$
$2\Delta_5\left[\sin k_x\tau_y\rho_x\sigma_x s_0-\sin k_y\tau_x\rho_x\sigma_x s_z\right]$	$\Delta_{13}\left[2\sin k_x\sin k_y\tau_x\rho_y\,(\sigma_0-\sigma_z)\,s_x\right]$
$\Delta_6\left[\sin k_x\tau_y\rho_0(\sigma_0-\sigma_z)s_0+\sin k_y\tau_x\rho_0(\sigma_0-\sigma_z)s_z\right]$	
$\Delta_7\left[\sin k_x\tau_y\rho_x(\sigma_0-\sigma_z)s_0+\sin k_y\tau_x\rho_x(\sigma_0-\sigma_z)s_z\right]$	

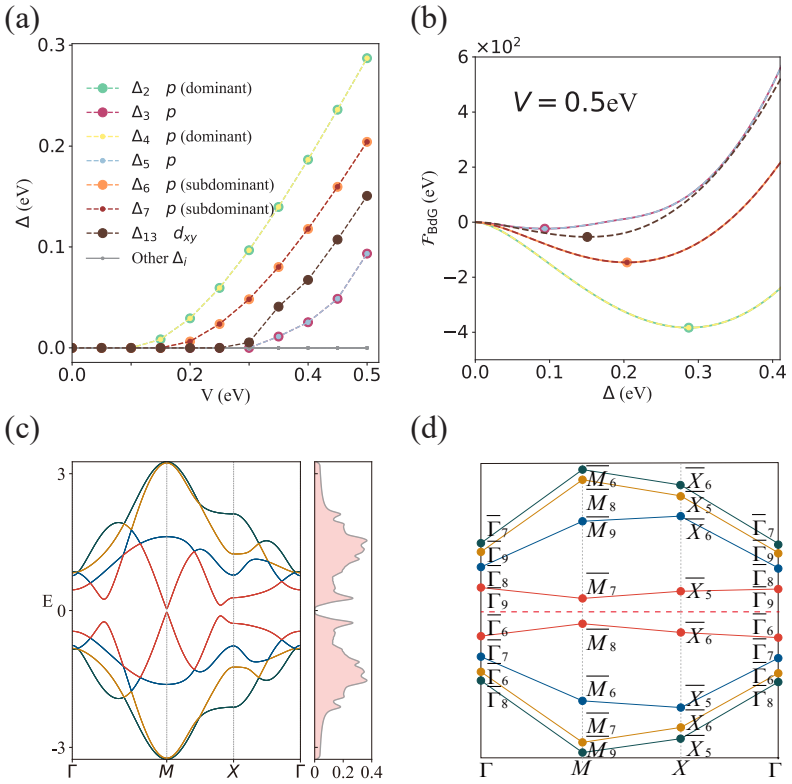

FIG. 9. (a) Pairing strength Δ_i vs V_i obtained by solving the self-consistent equations for B_{2u} pairing channel. The result shows that Δ_2 and Δ_4 pairing is the primarily favored, while the Δ_6 and Δ_7 pairings are secondly favored. (b) BdG condensation energy $\mathcal{F}_{\rm BdG}$ vs $|\Delta_i|$ at $V_i = 0.5$ eV. (c) Bulk spectrum of the superconducting state of $La_3Ni_2O_7$. (d) Band coreps of the bulk spectrum. The parameters are also $\Delta_2 = 0.3871102$, $\Delta_4 = 0.2871102$eV, $\Delta_6 = 0.3041629$eV, and $\Delta_7 = 0.2041629$eV.

17. DETAILS OF THE DFT CALCULATION

Density functional theory (DFT) calculations were performed by Vienna ab initio simulation package (VASP) [14, 15] with generalized gradient approximation (GGA) of PerdewBurke-Ernzerhof form (PBE) exchange correlation potential [16]. The projector augmented wave (PAW) [17, 18] method with a 600 eV plane-wave cutoff is applied. The lattice constants were fixed to experimental results at 29.5 GPa [19] and only the positions of inner atoms were optimized. The convergence criterion of force was set to 0.001 eV/Å and total energy convergence criterion was set to 10^{-7} eV with a Γ-centered $19 \times 19 \times 19$ k-mesh grid. An effective Hubbard U parameter $U = 3.5$ eV was employed to account for the correlation effects of 3d electrons in the Ni atoms [20, 21]. To obtain the projected tight-binding models, maximally localized Wannier functions as implemented in WANNIER90 [22] package are obtained, in which the good convergences were reached. Up to the next-nearest neighbors, the values of the tight-binding parameters of Eq. 1 in the main text are list in Tab. X.

TABLE X. Parameters of the tight-binding model in Eq. 1 in the main text. The values of the parameters can be obtained by Wannier fitting the band structure calculated by DFT.

t_1^x	t_1^z	t_2^x	t_2^z	t_3^{xz}
−0.511453	−0.123267	0.06746	−0.018433	−0.259349
$\epsilon_\perp^x$	$\epsilon_\perp^z$	t_4^{xz}	ϵ^x	ϵ^z
0.012643	−0.69961	0.033304	0.9337312	0.4115982
$t_\perp^z$				
0.022454				

* fenggh@lingnan.edu.cn
† quanj@lingnan.edu.cn

[1] S. Ono, Y. Yanase, and H. Watanabe, Symmetry indicators for topological superconductors, Phys. Rev. Res. **1**, 013012 (2019).
[2] A. Skurativska, T. Neupert, and M. H. Fischer, Atomic limit and inversion-symmetry indicators for topological superconductors, Phys. Rev. Res. **2**, 013064 (2020).
[3] S. Ono, H. C. Po, and H. Watanabe, Refined symmetry indicators for topological superconductors in all space groups, Science Advances **6**, eaaz8367 (2020).
[4] D. Varjas, T. O. Rosdahl, and A. R. Akhmerov, Qsymm: Algorithmic symmetry finding and symmetric Hamiltonian generation, New Journal of Physics **20**, 093026 (2018).
[5] Z. Zhang, Z.-M. Yu, G.-B. Liu, and Y. Yao, Magnetictb: A package for tight-binding model of magnetic and non-magnetic materials, Computer Physics Communications **270**, 108153 (2022).
[6] P. Coleman, Superconductivity and BCS theory, in *Introduction to Many-Body Physics* (Cambridge University Press, 2015) p. 486–541.
[7] T. Bzdušek and M. Sigrist, Robust doubly charged nodal lines and nodal surfaces in centrosymmetric systems, Physical Review B **96**, 155105 (2017).
[8] L. Elcoro, B. J. Wieder, Z. Song, Y. Xu, B. Bradlyn, and B. A. Bernevig, Magnetic topological quantum chemistry, Nature Communications **12**, 5965 (2021).
[9] J. Cano and B. Bradlyn, Band Representations and Topological Quantum Chemistry, Annual Review of Condensed Matter Physics **12**, 225 (2021).
[10] H. C. Po, A. Vishwanath, and H. Watanabe, Symmetry-based indicators of band topology in the 230 space groups, Nature Communications **8**, 1 (2017).
[11] B. Bradlyn, L. Elcoro, J. Cano, M. G. Vergniory, Z. Wang, C. Felser, M. I. Aroyo, and B. A. Bernevig, Topological quantum chemistry, Nature **547**, 298 (2017).
[12] M. I. Aroyo, A. Kirov, C. Capillas, J. M. Perez-Mato, and H. Wondratschek, Bilbao Crystallographic Server. II. Representations of crystallographic point groups and space groups, Acta Crystallographica Section A: Foundations of Crystallography **62**, 115 (2006).
[13] M. I. Aroyo, J. M. Perez-Mato, C. Capillas, E. Kroumova, S. Ivantchev, G. Madariaga, A. Kirov, and H. Wondratschek, Bilbao Crystallographic Server: I. Databases and crystallographic computing programs, Zeitschrift für Kristallographie - Crystalline Materials **221**, 15 (2006).
[14] G. Kresse and J. Furthmuller, Efficiency of ab-initio total energy calculations for metals and semiconductors using a plane-wave basis set, Computational Materials Science **6**, 15 (1996).
[15] G. Kresse and J. Furthmuller, Efficient iterative schemes for ab initio total-energy calculations using a plane-wave basis set, Physical Review B **54**, 11169 (1996).

[16] J. P. Perdew, K. Burke, and M. Ernzerhof, Generalized gradient approximation made simple, Phys. Rev. Lett. **77**, 3865 (1996).
[17] P. E. Blochl, Projector augmented-wave method, Physical Review B **50**, 17953 (1994).
[18] G. Kresse and D. Joubert, From ultrasoft pseudopotentials to the projector augmented-wave method, Physical Review B **59**, 1758 (1999).
[19] J. Li, D. Peng, P. Ma, H. Zhang, Z. Xing, X. Huang, C. Huang, M. Huo, D. Hu, Z. Dong, X. Chen, T. Xie, H. Dong, H. Sun, Q. Zeng, H.-k. Mao, and M. Wang, Identification of superconductivity in bilayer nickelate $La_3Ni_2O_7$ under high pressure up to 100 gpa, National Science Review , nwaf220 (2025).
[20] J. Yang, H. Sun, X. Hu, Y. Xie, T. Miao, H. Luo, H. Chen, B. Liang, W. Zhu, G. Qu, C.-Q. Chen, M. Huo, Y. Huang, S. Zhang, F. Zhang, F. Yang, Z. Wang, Q. Peng, H. Mao, G. Liu, Z. Xu, T. Qian, D.-X. Yao, M. Wang, L. Zhao, and X. J. Zhou, Orbital-dependent electron correlation in double-layer nickelate $La_3Ni_2O_7$, Nature Communications **15**, 4373 (2024).
[21] S. L. Dudarev, G. A. Botton, S. Y. Savrasov, C. J. Humphreys, and A. P. Sutton, Electron-energy-loss spectra and the structural stability of nickel oxide: An lsda+u study, Phys. Rev. B **57**, 1505 (1998).
[22] A. A. Mostofi, J. R. Yates, Y.-S. Lee, I. Souza, D. Vanderbilt, and N. Marzari, wannier90: A tool for obtaining maximally-localised wannier functions, Computer Physics Communications **178**, 685 (2008).